Available online at www.sciencedirect.com
SCIENCE DIRECT®
Comput. Methods Appl. Mech. Engrg. 193 (2004) 1529–1578
Computer methods in applied mechanics and engineering
www.elsevier.com/locate/cma

An introduction to computational nanomechanics and materials

W.K. Liu *,[1], E.G. Karpov, S. Zhang, H.S. Park

Department of Mechanical Engineering, Northwestern University, The Technological Institute, 2145 Sheridan Road, Evanston, IL 60208-3111, USA

Received 1 June 2003; received in revised form 15 October 2003; accepted 2 December 2003

Abstract

Many arenas of research are rapidly advancing due to a combined effort between engineering and science. In some cases, fields of research that were stagnating under the exclusive domain of one discipline have been imbued with new discoveries through collaboration with practitioners from the second discipline. In computational mechanics, we are particularly concerned about the technological engineering interest by combining engineering technology and basic sciences through modeling and simulations. These goals have become particularly relevant due to the emergence of the field of nanotechnology, and the related burst of interest in nanoscale research. In this introductory article, we first briefly review the essential tools used by nanoscale researchers. These simulation methods include the broad areas of quantum mechanics, molecular dynamics and multiple-scale approaches, based on coupling the atomistic and continuum models. Upon completing this review, we shall conclusively demonstrate that the atomistic simulation tools themselves are not sufficient for many of the interesting and fundamental problems that arise in computational mechanics, and that these deficiencies lead to the thrust of multiple-scale methods. We summarize the strengths and limitations of currently available multiple-scale techniques, where the emphasis is made on the latest perspective approaches, such as the bridging scale method, multi-scale boundary conditions, and multi-scale fluidics. Example problems, in which multiple-scale simulation methods yield equivalent results to full atomistic simulations at fractions of the computational cost, are shown. We conclude by discussing future research directions and needs in multiple-scale analysis, and also discuss the ramifications of the integration of current nanoscale research into education.

Keywords: Nanomechanics and materials; Multi-scale simulations

1. Introduction

The rapid advances in nanotechnology, nanomaterials and nanomechanics offer huge potentials in national defense, homeland security, and private industry. An emphasis on nanoscale entities will make our

* Corresponding author. Tel.: +1-847-491-7094; fax: +1-847-491-3915.
E-mail address: w-liu@northwestern.edu (W.K. Liu).
[1] Walter P. Murphy Professor of Mechanical Engineering.

0045-7825/$ - see front matter
doi:10.1016/j.cma.2003.12.008

manufacturing technologies and infrastructure more sustainable in terms of reduced energy usage and environmental pollution. Recent advances in the research community on this topic have stimulated ever-broader research activities in science and engineering devoted to their development and their applications.

With the confluence of interest in nanotechnology, the availability of experimental tools to synthesize and characterize systems in the nanometer scale, and computational tools widely accessible to model micro-scale systems by coupled continuum/molecular/quantum mechanics, we are poised to unravel the traditional gap between the atomic and the macroscopic world in mechanics and materials. This in turn opens up new opportunities in education and research.

Over the past three decades, we have acquired new tools and techniques to synthesize nanoscale objects and to learn their many incredible properties. Today's high-resolution electron microscopes can routinely see individual atoms. Scanning probe techniques allow us to manipulate atoms one at a time. Advanced materials synthesis provides the technology to tailor-design systems from as small as molecules to structures as large as the fuselage of a plane. We now have the technology to detect single molecules, bacteria or virus particles. We can make protective coatings more wear-resistant than diamond and fabricate alloys and composites stronger than ever before.

Advances in the synthesis of nanoscale materials have stimulated ever-broader research activities in science and engineering devoted entirely to these materials and their applications. This is due in large part to the combination of their expected structural perfection, small size, low density, high stiffness, high strength and excellent electronic properties. As a result, nanoscale materials may find use in a wide range of applications in material reinforcement, field emission panel display, chemical sensing, drug delivery, nanoelectronics and tailor-designed materials. Nanoscale devices have great potential as sensors and as medical diagnostic and delivery systems.

In most of these applications, nanoscale materials will be used in conjunction with other components that are larger, and have different response times, thus operating at different time and length scales. Single scale methods such as "ab initio" quantum mechanical methods or molecular dynamics (MD) will have difficulty in analyzing such hybrid structures due to the limitations in terms of the time and length scales that each method is confined to. Because of the availability of accurate interatomic potentials for a range of materials, classical MD simulations have become prominent as a tool for elucidating complex physical phenomena. However, the length and time scales that can be probed using MD are still fairly limited. For the study of nanoscale mechanics and materials, we must model up to a scale of several microns, consisting of billions of atoms, which is too large for MD simulations to-date. Hence, we need to develop multi-scale approaches for this class of problems. One possible approach that can be applied to many problems is to use MD only in localized regions in which the atomic-scale dynamics are important, and a continuum simulation method, such as the finite element [1–3] or meshfree [4–16] method, everywhere else. This general approach has been taken by several different groups using methods that have had varying degrees of success. In particular, these methods do not satisfactorily address the issue of disparate time scales in the two regions, and provide a rather simplified treatment of the interface between the atomistic and continuum regimes.

Current research in engineering is just beginning to impact molecular scale mechanics and materials and would benefit from interaction with basic sciences. For solids, research in the area of plasticity and damage has experienced some success in advancing micro-scale component design. Development of carbon nanotubes [17–31] is also an area in which nanoscale research has clearly played a major role. Other areas of opportunities include nanocomposites [32–38] and nanoalloys [39–42]. For fluids, coupling physics phenomena at the nanoscale is crucial in designing components at the micro-scale [43–48,151]. Electrophoresis and electro-osmotic flows coupled with particulate motion in a liquid have been important research areas that have had great impact in the homeland security area. Micro-fluidic devices often comprise components that couple chemistry, and even electrochemistry, with fluid motion. Once the physics-based models are determined for the solids and fluids, computational approaches will need to be employed or developed to capture the coupled physics phenomena.

The material presented in this review paper informs researchers and educators about specific fundamental concepts and tools in nanomechanics and materials, including solids and fluids. It is envisioned that this work will serve as a starting point from which interested researchers may jump into and contribute to the emerging field of computational nanotechnology.

The paper's outline is given by the following. Section 2 reviews the fundamentals of classical molecular dynamic simulations, such as the Lagrangian and Hamiltonian formulations, and the structure of interatomic potential functions. Section 3 informs the reader on the relevant quantum mechanical approaches and explains the energetic link between the quantum and classical systems. In Section 4, we outline the intrinsic limitations of molecular dynamic simulations and emphasize the necessity in developing the coupled multi-scale methods. Section 5 reviews available multi-scale approaches: hierarchical and concurrent coupling of the atomistic and continuum simulations (with the emphasis on the bridging scale method), multi-scale boundary conditions and multiple-scale fluidics. Section 6 concludes the paper by discussing future research needs in multiple-scale analysis, and the impact the current research has on the graduate curriculum at Northwestern.

2. Molecular dynamics

Molecular dynamics (MD) was first used in thermodynamics and physical chemistry to calculate the collective or average thermochemical properties of various physical systems including gases, liquids, and solids. It has been recently applied to simulate the instantaneous atomic behavior of a material system.

There are two basic assumptions made in standard molecular dynamics simulations [49–52]:

(1) Molecules or atoms are described as a system of interacting material points, whose motion is described dynamically with a vector of instantaneous positions and velocities. The atomic interaction has a strong dependence on the spatial orientation and distances between separate atoms. This model is often referred to as the soft sphere model, where the softness is analogous to the electron clouds of atoms.
(2) No mass changes in the system. Equivalently, the number of atoms in the system remains the same.

The simulated system is usually treated as an isolated domain system with conserved energy. However, non-conservative techniques [53–58] are available which model the dissipation of the kinetic energy into the surrounding media. These techniques will prove to be useful in the multiple-scale simulation methods presented later in this paper.

2.1. Lagrangian equations of motion

The equation of motion of a system of interacting material points (particles, atoms), having in total s degrees of freedom, can be most generally written in terms of a Lagrangian function L, e.g. [59,60]:

$$\frac{\mathrm{d}}{\mathrm{d}t}\frac{\partial L}{\partial \dot{q}_\alpha} - \frac{\partial L}{\partial q_\alpha} = 0, \quad \alpha = 1, 2, \ldots, s. \tag{1}$$

Here q are the generalized coordinates, the arbitrary observables that uniquely define spatial positions of the atoms, and the superposed dot denotes time derivatives. As will be discussed in Section 2.2, Eq. (1) can be rewritten in terms of the generalized coordinates and momenta, and successively utilized within the statistical mechanics formulation.

The molecular dynamics simulation is most typically run with reference to a Cartesian coordinate systems, where Eq. (1) can be simplified to give

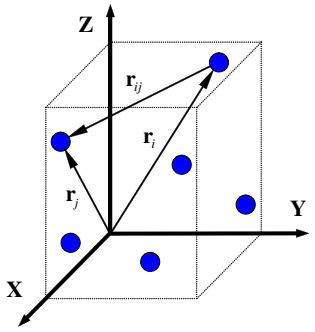

Fig. 1. Coordination in atomic systems.

$$\frac{\mathrm{d}}{\mathrm{d}t}\frac{\partial L}{\partial \dot{\mathbf{r}}_i} - \frac{\partial L}{\partial \mathbf{r}_i} = 0, \quad i = 1, 2, \ldots, N. \tag{2}$$

Here, $\mathbf{r}_i = (x_i, y_i, z_i)$ is the radius vector of atom i, Fig. 1, and N is the total number of simulated atoms, $N = s/3$ within the three-dimensional settings. The spatial volume occupied by these N atoms is usually referred to as the *MD domain*.

Due to the homogeneity of time and space, and also isotropy of space in inertial coordinate systems, the equations of motion (2) must not depend on the choice of initial time of observation, the origin of the coordinate system, and directions of its axes. These basic principles are equivalent to the requirements that the Lagrangian function cannot explicitly depend on time, directions of the radius and velocity vectors $\mathbf{r}_i$ and $\dot{\mathbf{r}}_i$, and it can only depend on the absolute value of the velocity vector $\dot{\mathbf{r}}_i$. In order to provide identical equations of motions in all inertial coordinate systems, the Lagrangian function must also comply with the Galilean relativity principle. One function satisfying all these requirements reads [60]

$$L = \sum_{i=1}^{N} \frac{m_i}{2}(\dot{x}_i^2 + \dot{y}_i^2 + \dot{z}_i^2) \equiv \sum_{i=1}^{N} \frac{m_i \dot{\mathbf{r}}_i^2}{2}, \tag{3}$$

for a system of free, non-interacting, particles; m_i is the mass of particle i.

Interaction between the particles can be described by adding to (3) a particular function of atomic coordinates U, depending on properties of this interaction. Such a function is defined with a negative sign, so that the system's Lagrangian acquires the form:

$$L = \sum_{i=1}^{N} \frac{m_i \dot{\mathbf{r}}_i^2}{2} - U(\mathbf{r}_1, \mathbf{r}_1, \ldots, \mathbf{r}_N), \tag{4}$$

where the two terms represent the system's kinetic and potential energy, respectively (note the additivity of the kinetic energy term). This gives the general structure of Lagrangian for a conservative system of interacting material points in Cartesian coordinates. It is important to note two features of this Lagrangian: *the additivity of the kinetic energy term and the absence of an explicit dependence on time*. The fact that the potential energy term only depends on spatial configuration of the particles implies that any change in this configuration results in an immediate effect on the motion of all particles within the simulated domain. The inevitability of this assumption is related to the relativity principle. Indeed, if such an effect propagated with a finite speed, the former would depend on the choice of an inertial system. In this case the laws of motion (in particular, the MD solutions) would be dissimilar in various systems; that would contradict the relativity principle.

By substituting the Lagrangian (4) to Eq. (2), the equations of motion can finally be written in the Newtonian form,

$$\boxed{m_i\ddot{\mathbf{r}}_i = -\frac{\partial U(\mathbf{r}_1,\mathbf{r}_2,\ldots,\mathbf{r}_N)}{\partial \mathbf{r}_i} \equiv \mathbf{F}_i, \quad i = 1,2,\ldots,N} \tag{5}$$

The force $\mathbf{F}_i$ is usually referred to as the *internal* force, i.e. the force exerted on atom i due to specifics of the environment it is exposed to. Eq. (5) are further solved for a given set of initial conditions to get trajectories of the atomic motion in the simulated system.

An important issue arising in MD simulations is accounting for a mechanism of the conduction of heat away from a localized area of interest. The MD domain is usually far too small to properly describe this process within a conservative system. Modern computer power allows modeling domains with a maximum of only several hundred million atoms; that corresponds to a material specimen of size only about $0.1\times0.1\times0.1$ μm. MD simulations are most often performed using periodic boundary conditions, implying that the total energy in the system remains constant; see Section 4 for detail. One common solution to this problem is to apply damping forces to a group of atoms along the boundaries of the MD domain. That is known as the heat bath technique, see Section 4.2 for detail. However, this approach cannot capture the true mechanism of dissipation in real systems. Furthermore, the potential energy term shown in Eq. (4), having no explicit dependence in time, implies the use of conservative models. According to some recent studies [56–58], *non-conservative* models can also be constructed, using this basic form of the Lagrangian and implementing the so-called "wave-transmitting" boundary conditions to describe energy dissipation from the molecular dynamics domain into the surrounding media. The basic idea of such an approach is to calculate the response of the outer region to excitations originating from the MD domain at each time step of the simulation. The outward heat flow is then cancelled due to negative work done by the corresponding response forces applied to boundary atoms within the localized area of interest.

The classical Lagrangian formulation, discussed in this section, is typically used for those molecular dynamics simulations aimed on the analysis of detailed atomic motion, rather than on obtaining averaged (statistical) characteristics [49]. In the latter case, the Hamiltonian formulation can be alternatively used, as will be discussed in Section 2.2.

2.2. Hamiltonian equations of motion

The Lagrangian formulation for the MD equations of motion discussed in Section 2.1 assumes description of the mechanical state of simulated system by means of generalized coordinates and velocities. This description, however, is not the only one possible. An alternative description, in terms of the generalized coordinates and momentum, is utilized within the Hamiltonian formulation, e.g. [59,60]. The former provides a series of advantages, particularly in studying general or averaged features of the simulated systems, such as the specifics of energy distribution and thermal flow, as well as in computing the physical observables (thermodynamic quantities), such as temperature, volume and pressure. In the latter case, the methods of statistical mechanics methods are employed, and those typically utilize the Hamiltonian formulation in describing the state and evolution of many-particle systems.

Transition to the new set of independent variables can be accomplished as the following. First employ the complete differential of the Lagrangian function of Eq. (1),

$$\mathrm{d}L = \sum_\alpha \frac{\partial L}{\partial q_\alpha}\mathrm{d}q_\alpha + \sum_\alpha \frac{\partial L}{\partial \dot{q}_\alpha}\mathrm{d}\dot{q}_\alpha, \quad \alpha = 1,2,\ldots,s, \tag{6}$$

and rewrite this as

$$\mathrm{d}L = \sum_\alpha \dot{p}_\alpha \mathrm{d}q_\alpha + \sum_\alpha p_\alpha \mathrm{d}\dot{q}_\alpha, \tag{7}$$

where the generalized momenta are defined to be

$$p_\alpha = \frac{\partial L}{\partial \dot{q}_\alpha}. \tag{8}$$

The right-hand side of Eq. (7) can be rearranged as

$$\mathrm{d}L = \sum_\alpha \dot{p}_\alpha \,\mathrm{d}q_\alpha + d\left(\sum_\alpha p_\alpha \dot{q}_\alpha\right) - \sum_\alpha \dot{q}_\alpha \,\mathrm{d}p_\alpha, \tag{9}$$

$$\mathrm{d}\left(\sum_\alpha p_\alpha \dot{q}_\alpha - L\right) = \sum_\alpha \dot{q}_\alpha \,\mathrm{d}p_\alpha - \sum_\alpha \dot{p}_\alpha \,\mathrm{d}q_\alpha, \tag{10}$$

where the function

$$H(p,q,t) = \sum_\alpha p_\alpha \dot{q}_\alpha - L \tag{11}$$

is referred to as the (classical) *Hamiltonian* of the system. The value of the Hamiltonian function is an integral of motion for conservative systems, and it is defined to be the total energy of the system in terms of the generalized coordinates and momenta.

Thus, we have obtained

$$\mathrm{d}H = \sum_\alpha \dot{q}_\alpha \,\mathrm{d}p_\alpha - \sum_\alpha \dot{p}_\alpha \,\mathrm{d}q_\alpha, \tag{12}$$

and therefore

$$\dot{q}_\alpha = \frac{\partial H}{\partial p_\alpha}, \quad \dot{p}_\alpha = -\frac{\partial H}{\partial q_\alpha}. \tag{13}$$

These are the Hamiltonian equations of motion in terms of new variable p and q. They comprise a system of $2s$ first-order ODEs on $2s$ unknown functions $p(t)$ and $q(t)$. A set of values of these functions at a given time represents the state of the system at this time. This set can also be viewed as a vector in a $2s$-dimensional vector space known as the *phase* space. A complete set of these vectors, observed in the course of temporal evolution of the system, defines a hyper-surface in the phase space, known as the *phase space trajectory*. The phase space trajectory provides a complete description of the system's dynamics.

Although both the kinetic and potential energies do usually vary or fluctuate in time, the phase space trajectory determined from Eq. (13) conserves the total energy of the system. Indeed, the time rate of change of the Hamiltonian is equal to zero,

$$\frac{\mathrm{d}H}{\mathrm{d}t} = \frac{\partial H}{\partial t} + \sum_\alpha \frac{\partial H}{\partial q_\alpha}\dot{q}_\alpha + \sum_\alpha \frac{\partial H}{\partial p_\alpha}\dot{p}_\alpha = \frac{\partial H}{\partial t} = 0 \tag{14}$$

since it has no explicit dependence on time in the case of a conservative system, as follows from (11) and (3).

For a conservative system of N interacting atoms in a Cartesian coordinate system, the Hamiltonian description acquires the following form:

$$H(\mathbf{r}_1, \mathbf{r}_2, \ldots, \mathbf{r}_N, \mathbf{p}_1, \mathbf{p}_2, \ldots, \mathbf{p}_N) = \sum_i \frac{\mathbf{p}_i^2}{2m_i} + U(\mathbf{r}_1, \mathbf{r}_2, \ldots, \mathbf{r}_N), \tag{15}$$

$$\boxed{\dot{\mathbf{r}}_i = \frac{\partial H}{\partial \mathbf{p}_i}, \quad \dot{\mathbf{p}}_i = -\frac{\partial H}{\partial \mathbf{r}_i}}, \tag{16}$$

where the momenta are related to the radius vectors as $\mathbf{p}_i = m_i \dot{\mathbf{r}}_i$.

If the Hamiltonian function and an initial state of the atoms in the system are known, one can compute the instantaneous positions and momentums of the atoms at all successive times, solving Eq. (16). That gives the phase space trajectory of the atomic motion, which can be of particular importance in studying the dynamic evolution of atomic structure and bonds, as well as the thermodynamic states of the system. We note, however, that the Newtonian equation (5), following from the Lagrangian formulation (1), can be more appropriate in studying particular details of the atomistic processes, especially in solids. The Newtonian formulation is usually more convenient in terms of imposing external forces and constraints (for instance, periodic boundary conditions), as well as the post-processing and visualization of the results.

2.3. Interatomic potentials

According to Eq. (5), the general structure of the governing equations for molecular dynamics simulations is given by a straightforward second-order ODE. However, the potential function for (5) can be an extremely complicated object, when accurately representing the atomic interactions within the simulated system. The nature of this interaction is due to complicated quantum effects taking place at the subatomic level that are responsible for chemical properties such as valence and bond energy; quantum effects also are responsible for the spatial arrangement (topology) of the interatomic bonds, their formation and breakage. In order to obtain reliable results in molecular dynamic simulations, the classical interatomic potential should accurately account for these quantum mechanical processes, though in an averaged sense, as outlined in Section 3.

The issues related to the form of the potential function for various classes of atomic systems have been extensively discussed in literature. The general structure of this function is presented by the following:

$$U(\mathbf{r}_1, \mathbf{r}_2, \ldots, \mathbf{r}_N) = \sum_i V_1(\mathbf{r}_i) + \sum_{i,j>i} V_2(\mathbf{r}_i, \mathbf{r}_j) + \sum_{i,j>i,k>j} V_3(\mathbf{r}_i, \mathbf{r}_j, \mathbf{r}_k) + \cdots, \tag{17}$$

where $\mathbf{r}_n$ is the radius vector of the nth particle, and function V_m is called the m-body potential. The first term of (17) represents the energy due an external force field, such as gravitational or electrostatic, which the system is immersed into; the second shows pair-wise interactions of the particles, the third gives the three-body components, etc. In practice, the external field term is usually ignored, while all the multi-body effects are incorporated into V_2 in order to reduce the computational expense of the simulations.

2.3.1. Two-body (pair) potentials

At the subatomic level, the electrostatic field due to the positively charged atomic nucleus is neutralized by the negatively charged electron clouds surrounding the nucleus. Within the quantum mechanical description of electron motion, a probabilistic approach is employed to evaluate the probability densities at which the electrons can occupy particular spatial locations. The term "electron cloud" is typically used in relation to spatial distributions of these densities.

The negatively charged electron clouds, however, experience cross-atomic attraction, which grows as the distance between the nuclei decreases. On reaching some particular distance, which is referred to as the equilibrium bond length, this attraction is equilibrated by the repulsive force due to the positively charged nuclei. A further decrease in the internuclei distance results in a quick growth of the resultant repulsive force.

There exist a variety of mathematical models to describe the above physical phenomena. In 1924, Jones [61,62] proposed the following potential function to describe pair-wise atomic interactions:

$$V(\mathbf{r}_i, \mathbf{r}_j) = V(r) = 4\varepsilon\left[\left(\frac{\sigma}{r}\right)^{12} + -\left(\frac{\sigma}{r}\right)^{6}\right], \quad r = |\mathbf{r}_{ij}| = |\mathbf{r}_i - \mathbf{r}_j|. \tag{18}$$

This model is currently known as the *Lennard–Jones* (LJ) potential, and it is used in simulations of a great variety of atomistic systems and processes. Here, $\mathbf{r}_{ij}$ is the interatomic radius-vector, see Fig. 1, σ is the collision diameter, the distance at which $V(r) = 0$, and ε shows the bonding/dislocation energy—the minimum of function (18) to occur for an atomic pair in equilibrium. The first term of this potential represents atomic repulsion, dominating at small separation distances while the second term shows attraction (bonding) between two atoms. Since the square bracket quantity is dimensionless, the choice of units for V depends on the definition of ε. Typically, $\varepsilon \sim 10^{-19}, \ldots, 10^{-18}$ joule (J), therefore it is more convenient to use a smaller energy unit, such as electron volt (eV), rather than joules. $1\ \text{eV} = 1.602 \times 10^{-19}$ J, which represents the work done if an elementary charge is accelerated by an electrostatic field of a unit voltage. The energy ε represents the amount of work that needs to be done in order to remove one of two coupled atoms from its equilibrium position ρ to infinity. The value ρ is also known as the equilibrium bond length, and it is related to the collision diameter as $\rho = \sqrt[6]{2}\sigma$. In a typical atomistic system, the collision diameter σ is equal to several angstroms (Å), $1\ \text{Å} = 10^{-10}$ m.

The corresponding force between the two atoms can be expressed as a function of the interatomic distance,

$$F(r) = -\frac{\partial V(r)}{\partial r} = 24\frac{\varepsilon}{\sigma}\left[2\left(\frac{\sigma}{r}\right)^{13} - \left(\frac{\sigma}{r}\right)^{7}\right]. \tag{19}$$

The potential and force functions (18) and (19) are plotted versus the interatomic distance in Fig. 2a, using dimensionless quantities.

Another popular model for pair-wise interactions is known as the Morse potential, Fig. 2b:

$$V(r) = \varepsilon[e^{2\beta(\rho-r)} - 2e^{\beta(\rho-r)}], \quad F(r) = 2\varepsilon\beta[e^{2\beta(\rho-r)} - e^{\beta(\rho-r)}], \tag{20}$$

where ρ and ε are the equilibrium bond length and dislocation energy respectively; β is an inverse length scaling factor. Similar to the Lennard–Jones model, the first term of this potential is repulsive and the second is attractive, which is interpreted as representing bonding. The Morse potential (20) has been adapted for modeling atomic interaction in various types of materials and interfaces; examples can be found elsewhere [63,64].

The Lennard–Jones and Morse potentials are most commonly used in molecular dynamics simulations, based on the pair-wise approximation, in chemistry, physics and engineering.

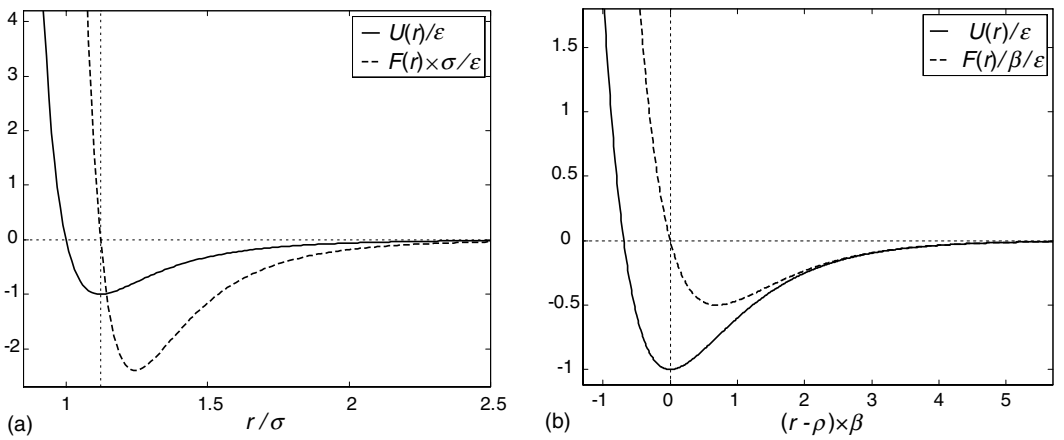

Fig. 2. Pair-wise potentials and the interatomic forces: (a) Lennard–Jones, (b) Morse.

2.3.2. Cut-off radius of the potential function

One important issue arising from molecular dynamics simulations relates to the truncation of the potential functions, such as (18) and (20). Note that computing the internal force for the equations of motion (5) due only to pair-wise interaction requires $(N^2 - N)/2$ terms, where N is the total number of atoms. This value corresponds to the case when one takes into account the interaction of each current atom i with all other simulated atoms $j \neq i$; this can be expensive even for considerably small systems. Assuming that the current atom interacts with just its nearest neighbors can reduce the computational effort significantly. Therefore, a *cut-off radius*, R, is typically introduced and defined as some maximum value of the modulus of the radius vector. The truncated pair-wise potential can then be written as the following:

$$V^{(\mathrm{tr})}(r) = \begin{cases} V(r) & r \leqslant R, \\ 0 & r > R. \end{cases} \tag{21a}$$

If each atom interacts with only n atoms in its R-vicinity, the evaluation of the internal pair-wise forces will involve $nN/2$ terms.

To assure continuity (differentiability) of V, according to (5), a"skin" factor can be alternatively introduced for the truncated potential by means of a smooth step-like function f_c, which is referred to as the *cut-off function*,

$$V^{(\mathrm{tr})}(r) = f_c(r)V(r), \tag{21b}$$

f_c assures a smooth and quick transition from 1 to 0 when the value of r approaches R, and is usually chosen to take the form of a simple analytical function of the interatomic distance r. One example of a trigonometric cut-off function is shown in Eq. (25) of Section 2.3.3.

2.3.3. Multi-body interaction

The higher-order terms of the potential function (17) are typically employed in simulations of solids and complex molecular structures to account for chemical bond formation, their topology and spatial arrangement, as well as the chemical valence of atoms. However, practical implementation of the multi-body interaction can be extremely involved. As a result, all the multi-body terms of the order higher than three are usually ignored.

Essentially, the three-body potential V_3 is intended to provide contributions to the potential energy due to the change of angle between radius vectors $\mathbf{r}_{ij} = \mathbf{r}_i - \mathbf{r}_j$, in addition to the change of absolute values $|\mathbf{r}_{ij}|$. This accounts for changes in molecular shapes and bonding geometries in atomistic structure, e.g. [65,66].

However, the general three-body potentials, such as V_3 in Eq. (17), have been criticized for their inability to describe the energetics of all possible bonding geometries [67–69], while a general form for a four- and five-body potential appears intractable, and would contain too many free parameters. As a result, a variety of advanced two-body potentials have been proposed to efficiently account for the specifics of a *local* atomistic environment by incorporating some particular multi-body dependence inside the function V_2, known as *bond-order* functions, rather than introducing the multi-body potential functions $V_{m>2}$. These terms implicitly include the angular dependence of interatomic forces by introducing the so-called bond-order function, while the overall pair-wise formulation is preserved. Also, these potentials are usually treated as short-range ones, i.e. accounting for interaction between a current atom and several neighbors only. Some of the most common models of this type are the following: the Tersoff potential [69–71] for a class of covalent systems, such as carbon, silicon and germanium, the Brenner [72–74] and REBO [75] potentials for carbon and hydrocarbon molecules, and the Finnis–Sinclair potential for BCC metals [76,77].

In spite of the variety of existing local environment potentials, all of them feature a common overall structure, given by the following expression:

$$V_2(\mathbf{r}_i, \mathbf{r}_j) \equiv V_{ij} = (V_{\mathrm{R}}(r_{ij}) - B_{ij} V_{\mathrm{A}}(r_{ij})), \quad r_{ij} = |\mathbf{r}_{ij}|, \tag{22}$$

where V_{R} and V_{A} are pair-wise repulsive and attractive interactions, respectively, and the bond-order function B is intended to represent the multi-body effects by accounting for spatial arrangements of the bonds in a current atom's vicinity.

The silicon potential model by Tersoff [69] gives an example of the local environment approach:

$$V_{ij} = f_{\mathrm{c}}(r_{ij})(A\mathrm{e}^{-\lambda_1 r_{ij}} - B_{ij}\mathrm{e}^{-\lambda_2 r_{ij}}), \tag{23a}$$

$$\begin{aligned} B_{ij} &= (1 + \beta^n \zeta_{ij}^n)^{-1/2n}, \\ \zeta_{ij} &= \sum_{k \neq i,j} f_{\mathrm{c}}(r_{ik}) g(\theta_{ijk}) \mathrm{e}^{\lambda_2^3 (r_{ij} - r_{ik})^3}, \\ g(\theta) &= 1 + c^2/d^2 - c^2/[d^2 + (h - \cos\theta)^2]. \end{aligned} \tag{23b}$$

Here, the cutoff function is chosen as

$$f_{\mathrm{c}}(r) = \frac{1}{2} \begin{cases} 2 & r < R - D, \\ 1 - \sin(\pi(r - R)/2D) & R - D < r < R + D, \\ 0 & r > R + D, \end{cases} \tag{24}$$

where the middle interval function is known as the "skin" of the potential. Note that if the local bond-order is ignored, so that $B = 2A = \mathrm{const}$, and $\lambda_1 = 2\lambda_2$, potential (23) reduces to the Morse model (20) at $r < R - D$. In other words, all deviations from a simple pair potential are ascribed to the dependence of the function B on the local atomic environment. The value of this function is determined by the number of competing bonds, the strength λ of the bonds and the angles θ between them (θ_{ijk} shows the angle between bonds ij and ik). The function ζ of (23) is a weighted measure of the number of bonds competing with the bond i–j, and the parameter n shows how much the closer neighbors are favored over more distant ones in the competition to form bonds.

The potentials proposed by Brenner and co-workers [72,75] are usually viewed as more accurate, though more involved, extensions of the Tersoff models [69–71]. The Brenner potentials include more detailed terms V_{A}, V_{R} and B_{ij} to account for different types of chemical bonds that occur in the diamond and graphite phases of the carbon, as well in hydrocarbon molecules.

Another special form of the multi-body potential is provided by the *embedded atom method* (EAM) for metallic systems [78–80]. One appealing aspect of the EAM is its physical picture of metallic bonding, where each atom is embedded in a host electron gas created by all neighboring atoms. The atom-host interaction is inherently more complicated than the simple pair-wise model. This interaction is described in a cumulative way, in terms of an empirical *embedding energy function*. The embedding function incorporates some important many-atom effects by providing the amount of energy (work) required to insert one atom into the electron gas of a given density. The total potential energy U includes the embedding energies G of all of atoms in the system, and the electrostatic pair-wise interaction energies V:

$$U = \sum_i G_i \left(\sum_{j \neq i} \rho_j^{\mathrm{a}}(r_{ij}) \right) + \sum_{i,j>i} V_{ij}(r_{ij}). \tag{25}$$

Here, ρ_j^{a} is the averaged electron density for a host atom j, viewed as a function of the distance between this atom and the embedded atom i. Thus, the host electron density is employed as a linear superposition of contributions from individual atoms, which in turn are assumed to be spherically symmetric. The embedded atom method has been applied successfully to studying defects and fracture, grain boundaries, interdiffusion in alloys, liquid metals, and other metallic systems and processes [78].

3. Energetic link between MD and quantum mechanics

Within the molecular dynamics method, the interacting particles are viewed either as material points exerting potential forces into their vicinity, or as solid spheres with no internal structure. In other words, the internal state of the atoms and molecules does not vary in the course of the simulation, and there is no energy exchange between the MD system and the separate subatomic objects, the electrons and nuclei. However, each of the atoms within the MD system represents a complicated physical domain that can evolve in time and switch its internal state by exchanging energy with the surrounding media. Most importantly, the nature of averaged interatomic forces that are employed in the MD simulations is in fact determined by characteristics of the subatomic processes and states.

The dependence of the potential function U on the separation between atoms and molecules and their mutual orientation can in principle be obtained from quantum mechanical (QM) calculations. The further use of this function within a classical MD simulation provides an "energetic link" between the atomistic and subatomic scales. These arguments are employed in any multiscale approach designed to accurately relate the MD and QM simulations. Indeed, in the absence of information about the trajectories of particles within a quantum mechanical model, the energy arguments are solely appropriate for establishing the exchange of the information between the MD and QM subsystems.

To illustrate the general idea of MD/QM coupling, consider a simple example with two interacting hydrogen atoms. Those comprise one hydrogen molecule H_2, which consists of two proton nuclei (+) and two electrons (−). The positions of the electrons with respect to each other and the nuclei are defined by the lengths r_{12} and $r_{\alpha i}$, $\alpha = a, b$, $i = 1, 2$, and the separation distance between two atoms is given by r, as depicted in Fig. 3.

Obviously, the total energy E of this system consists of the energies of two unbound hydrogen atoms, E_a and E_b, plus an atomic binding energy term U,

$$E = E_a + E_b + U. \tag{26}$$

Since the classical MD models assume no energy absorption by the simulated atoms, the values E, E_a and E_b should relate to the atomic states with minimum possible energies, i.e. the so-called *ground states*. Provided that these energies are known from quantum mechanical calculations, and the full energy of the coupled system is available for various values r, one obtains a dependence $E(r)$, and therefore the energy of pair-wise atomic interactions as a function of r:

$$U(r) \equiv V_2(r) = E(r) - E_a - E_b. \tag{27}$$

When necessary, this function can be interpolated with a smooth curve, and next utilized in the classical molecular dynamics equations of motion (5) or (15) and (16); that is the general idea of establishing the link between the quantum mechanical and MD simulations.

The energies E_a and E_b can be found by solving the stationary Schrödinger wave equation [81–84] for each non-interacting hydrogen atom, i.e. when they are formally put at the infinite separation distance, $r \to \infty$. This equation gives the functional eigenvalue problem

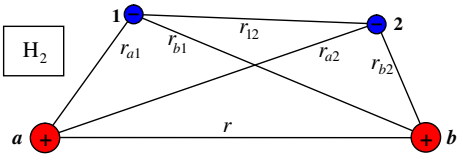

Fig. 3. Coordination in the hydrogen molecule.

$$\hat{h}\psi_\alpha = E_\alpha \psi_\alpha, \tag{28a}$$

$$\hat{h} = -\frac{\hbar^2}{2m}\Delta_\alpha - \frac{e^2}{r_\alpha}, \quad \Delta_\alpha = \frac{\partial^2}{\partial r^2}, \quad \alpha = a, b. \tag{28b}$$

Here $\hbar$, m and e are Planck's constant, the electron mass and charge, respectively; Δ is the Laplace operator, and $r_a \equiv r_{a1}$, $r_b \equiv r_{b2}$. $\hat{h}$ is the one-electron *Hamiltonian operator*. This operator resembles the Hamiltonian function of classical dynamics (15) which represents the total energy of a system in terms of the coordinates and momenta of the particles. Similarly, the first term in (28b) is the kinetic energy operator, and the second term gives the Coulomb potential of the electrostatic electron-proton interaction. Obviously, $E_a = E_b$ and $\psi_a = \psi_b$ for two identical atoms in the ground states. We will nevertheless preserve the above notation for generality, because similar arguments hold also for a pair of distinct atoms.

The wave function solution, such as ψ_α, provides the complete description of a quantum mechanical system in the corresponding energy state. At the same time, the wave function itself gives no immediate physical insight. It serves as a mathematical tool only and cannot be determined experimentally. It is used in further calculations in order to obtain observable quantities. For instance, the product $\psi_\alpha^* \psi_\alpha$, where the star notation means complex conjugate, provides a real-valued probability-density function of electron. Its integration over a spatial domain in the vicinity of the nucleus of the unbound atom α results in the probability of finding the electron in this spatial domain. The one-electron wave function ψ_α is often referred to as the hydrogen *atomic orbital*. All hydrogen orbitals and the corresponding energy levels are known in closed form that can be found elsewhere in quantum mechanics textbooks [81–84].

In principle, the full energy E of the bound diatomic system H_2 in the ground state can be obtained for a given separation distance r between the nuclei by solving the molecular two-electron Schrödinger equation,

$$\hat{H}\Psi = E\Psi, \tag{29}$$

$$\hat{H} = -\frac{\hbar^2}{2m}\Delta - \sum_{\alpha,i}\frac{e^2}{r_{\alpha i}} + \frac{e^2}{r_{12}} + \frac{e^2}{r}, \tag{30}$$

where the Laplacian Δ involves all the electronic degrees of freedom, and $\hat{H}$ and Ψ are the molecular Hamiltonian and the two-electron wave function, describing the ground state of the coupled system.

Remark: the protons are usually taken stationary at the distance r; that is known as the *Born–Oppenheimer approximation* in quantum mechanics, e.g. [81,85]. This approximation holds with a high accuracy, because the proton is 1800 times more massive than the electron. As far as r is a constant parameter in (30), the solution to (30) will be only in terms of the electronic coordinates $r_{\alpha i}$ and r_{12}.

Though the complete Hamiltonian $\hat{H}$ for any complex molecule is easily determined (see textbooks on quantum chemistry [85–88]), solving the resultant Schrödinger equation is usually difficult even for simple cases, such as the hydrogen molecule discussed. A variety of numerical methods have been developed to obtain approximate multi-atom/multi-electron wave functions. Some of these methods are outlined in Sections 3.1 and 3.2. The tight binding method utilizes the exact hydrogen orbitals to give the so-called *molecular orbital* $\tilde{\psi}$, an approximate wave function solution for a *single* electron interacting with several arbitrarily arranged nuclei. The Hartree–Fock and related methods employ these molecular orbitals to provide an approximate wave function $\tilde{\Psi}$ for the entire molecule, i.e. for several electrons interacting with the same group of nuclei. In principle, the tight binding method "adds nuclei/atoms", while the Hartree–Fock method "adds the electrons" to the hydrogen-like system. The molecular shape can also be investigated by finding the configuration with a minimum of the total energy.

In all cases, when an approximate N-electron wave function $\tilde{\Psi}$ is available, the total energy of the system can be computed as an integral over the electronic variables, instead of directly solving the Schrödinger equation (29). For the H_2 molecule, it gives

$$E \approx \frac{\int \ldots \int \tilde{\Psi}^* \hat{H} \tilde{\Psi} \, \mathrm{d}r_{a1}, \ldots, \mathrm{d}r_{b2} \, \mathrm{d}r_{12}}{\int \ldots \int \tilde{\Psi}^* \tilde{\Psi} \, \mathrm{d}r_{a1}, \ldots, \mathrm{d}r_{b2} \, \mathrm{d}r_{12}}, \tag{31a}$$

where the star notation implies the complex conjugate. The formula (31a) is obtained by premultiplying the wave equation (29) with the complex conjugate solution $\tilde{\Psi}^*$ and integrating it over all electronic degrees of freedom. The configuration integrals, such as those in (31), are usually written in quantum mechanics concisely as

$$E \approx \frac{\langle \tilde{\Psi} | \hat{H} | \tilde{\Psi} \rangle}{\langle \tilde{\Psi} | \tilde{\Psi} \rangle}, \tag{31b}$$

which implies integration over all electronic coordinates. According to (27) and (31b), the MD/QM linkage then gives

$$U(r) = \frac{\langle \tilde{\Psi}(r) | \hat{H} | \tilde{\Psi}(r) \rangle}{\langle \tilde{\Psi}(r) | \tilde{\Psi}(r) \rangle} - E_a - E_b, \tag{32}$$

where the polyatomic multi-electron wave function $\tilde{\Psi}$ depends on the interatomic distance r parametrically. Finally, the system of coupled MD/QM equations can be expressed as

$$\boxed{\hat{H}\Psi = \left(U + \sum_{\alpha} E_{\alpha} \right) \Psi, \quad m_i \ddot{\mathbf{r}}_i = -\frac{\partial U}{\partial \mathbf{r}_i}} \tag{33}$$

which represents the *concurrent* coupling between the subatomic and atomistic simulations of nanostructured systems (for more details, see [143]).

The density functional methods, Section 3.3, are based on alternative arguments. Instead of evaluating the multi-electron wave function, an approximate *electron density function* $\rho(\mathbf{r})$ is derived to give the probability density of finding electrons in the vicinity of a group of nuclei. In contrast to the molecular wave function, the function $\rho(\mathbf{r})$ of any system depends only on three spatial variables, the components of a radius vector x, y and z. Deriving a proper form of $\rho(\mathbf{r})$ is an important intermediate task in this method. The ground state energy E of a molecular system is then found as a functional operator over $\rho(\mathbf{r})$ without involving the multi-electron wave function formulation. Collectively, the density functional and Hartree–Fock methods are often referred to as the ab initio methods.

3.1. Tight binding method

The tight binding method, or the method of linear combination of atomic orbitals (LCAO) was originally proposed by Bloch [89] and later revised by Slater and Koster [90] in the context of periodic potential problems. The objective of this method is to construct an approximate wave function of a *single* electron in a non-central field due to two or more point sources (nuclei). Such a wave function is referred to as the molecular orbital (MO) and is further used in obtaining approximate trial functions for the corresponding multi-electron systems within the Hartree–Fock and related methods, Section 3.2.

The tight binding method is based on the assumption that the molecular orbital can be approximated as a linear combination of the corresponding atomic orbitals, i.e. from the readily available hydrogen type orbitals for each of the nuclei comprising the given molecular configuration. For the hydrogen ion H_2^+,

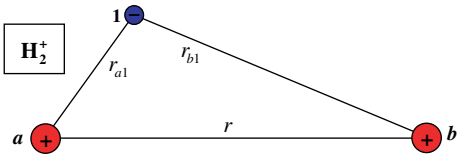

Fig. 4. Coordination in the hydrogen ion.

Fig. 4, consisting of two proton nuclei and one electron, the tight binding method provides the following approximate molecular orbital, e.g. [86,87]:

$$\tilde{\psi} = c_a\psi_a + c_b\psi_b. \tag{34}$$

The physical interpretation of this approximation is that in the vicinities of nuclei a and b, the sought molecular orbital should resemble the atomic orbitals ψ_a and ψ_b respectively.

According to the *variational principle* of quantum mechanics, the energy for a given (chosen) approximate wave function is always greater than for the true, or a more accurate, wave function. Therefore, the coefficients c_a and c_b for (34) can be found by minimizing the integral (31). Due to (31) and (34), the approximate ground state energy $\tilde{E} \geqslant E$ gives

$$\tilde{E} = \frac{\langle\tilde{\psi}|\hat{h}|\tilde{\psi}\rangle}{\langle\tilde{\psi}|\tilde{\psi}\rangle} = \frac{c_a^2 H_{aa} + c_b^2 H_{bb} + 2c_a c_b H_{ab}}{c_a^2 + c_b^2 + 2c_a c_b S_{ab}}, \tag{35}$$

where

$$S_{\alpha\beta} = \langle\psi_\alpha|\psi_\beta\rangle, \quad H_{\alpha\beta} = \langle\psi_\alpha|\hat{h}|\psi_\beta\rangle, \quad \alpha = a,b \text{ and } \beta = a,b, \tag{36}$$

$$\hat{h} = -\frac{\hbar^2}{2m}\Delta - \frac{e^2}{r_{a1}} - \frac{e^2}{r_{b1}} + \frac{e^2}{r}, \tag{37}$$

$\hat{h}$ is the Hamiltonian operator for a single electron in the field of two protons and r is the separation between two protons. In deriving (35), it was also assumed that the atomic orbitals obey the *normalization condition*

$$S_{\alpha\alpha} = \langle\psi_\alpha|\psi_\alpha\rangle = 1 \tag{38}$$

as well as the symmetries $S_{\alpha\beta} = S_{\beta\alpha}$ and $H_{\alpha\beta} = H_{\beta\alpha}$ that hold for the hydrogen ion.

At the variational minimum, we have the conditions $\partial\tilde{E}/\partial c_a = 0$, $\partial\tilde{E}/\partial c_b = 0$. Employing these conditions and the symmetry $H_{aa} = H_{bb}$, we obtain

$$c_a^2 - c_b^2 = 0, \tag{39}$$

which is only possible when

$$c_a = c_b \quad \text{or} \quad c_a = -c_b. \tag{40}$$

Thus, there exist two molecular orbitals for the H_2^+ ion, one symmetric and one antisymmetric:

$$\tilde{\psi}^{(+)} = N^{(+)}(\psi_a + \psi_b), \qquad \tilde{\psi}^{(-)} = N^{(-)}(\psi_a - \psi_b), \tag{41}$$

where $N^{(\pm)}$ are normalization factors, which can be found from the condition similar to (38). According to (40) and (35) these molecular states are characterized by the energies

$$\tilde{E}^{(+)} = \frac{H_{aa} + H_{ab}}{1 + S_{ab}}, \qquad \tilde{E}^{(-)} = \frac{H_{aa} - H_{ab}}{1 - S_{ab}}. \tag{42}$$

3.2. Hartree–Fock and related methods

In this section, we outline a group of numerical methods enabling one to build the ground state *multi-electron* wave function $\tilde{\Psi}$ based on either the exact hydrogen wave functions ψ_α or the approximate one-electron molecular orbitals $\tilde{\psi}$ of the type (41). The hydrogen wave functions are used for solving multi-electron systems in a central field, and the molecular orbitals—for polyatomic multi-electron systems, in particular, H_2. For both types of input wave functions, we will use the unified notation ψ_i, where the subscript index denotes the number of the electron in the system.

One commonly used approach is the approximation of *independent electrons*, which is equivalent to ignoring the term e^2/r_{12} in the Hamiltonian (30). This approximation gives the two-electron wave function as the second-order *Slater determinant*,

$$\tilde{\Psi} = \frac{1}{\sqrt{2}}\begin{vmatrix} \psi_1(1) & \psi_2(1) \\ \psi_1(2) & \psi_2(2) \end{vmatrix} = \frac{1}{\sqrt{2}}(\psi_1(1)\psi_2(2) - \psi_1(2)\psi_2(1)), \tag{43a}$$

where $\psi_i(j)$ is the wave function of electron i written in terms of the variables of electron j. For a multi-electron system, one obtains the N-order determinant,

$$\tilde{\Psi} = \frac{1}{\sqrt{N!}}\begin{vmatrix} \psi_1(1) & \psi_2(1) & \dots & \psi_N(1) \\ \psi_1(2) & \psi_2(2) & \dots & \psi_N(2) \\ \vdots & \vdots & & \vdots \\ \psi_1(N) & \psi_2(N) & \dots & \psi_N(N) \end{vmatrix}, \tag{43b}$$

where N is the total number of electrons in the system.

The functions (43) comply with the Pauli principle, stating that two electrons cannot simultaneously exist in the same one-electron state. Indeed, if for example $\psi_i(1) = \psi_j(2)$ at $i \neq j$, then the Slater determinant becomes trivial to indicate that such a state does not occur. As a result, the tight binding molecular orbitals (34), if used in (43), may require additional terms describing non-ground (excited) states of the hydrogen atom.

The electron–electron interaction can be taken into account with the use of the *Hartree method* [91]. Similar to the tight binding method, the variational principle is invoked to assume that the ground state energy for a chosen approximate wave function is always greater than for a more accurate wave function. The trial (zero-order) function can be adopted from the independent electron assumption, in particular:

$$\tilde{\Psi} = \psi_1^{(0)}(1)\psi_2^{(0)}(2), \tag{44}$$

where $\psi_i^{(0)}$ are the one-electron hydrogen eigenfunctions found by solving (28), or the tight-binding molecular orbitals according to (41). More accurate one-electron orbitals for (44) are next sought, in order to minimize the integral (31). This minimization problem reduces to the iteration procedure, where the updated orbitals are found by solving the system of one-electron Schrödinger equations,

$$\left[-\frac{\hbar^2}{2m}\Delta - \sum_\alpha \frac{e^2}{r_{\alpha i}} + \frac{e^2}{r} + \chi_i^{(0)} - E_i \right]\psi_i^{(1)} = 0, \quad i = 1, 2, \dots, N \tag{45}$$

with the energy integrals χ_i involving the trial orbitals of (44),

$$\chi_i^{(0)} = \sum_{j \neq i} \left\langle \psi_j^{(0)} \middle| \frac{e^2}{r_{ij}} \middle| \psi_j^{(0)} \right\rangle, \quad i = 1, 2, \dots, N, \tag{46a}$$

where r_{ij} are the interelectron distances. For a two-electron system, one obtains

$$\chi_1^{(0)} = \left\langle \psi_2^{(0)} \middle| \frac{e^2}{r_{12}} \middle| \psi_2^{(0)} \right\rangle, \qquad \chi_2^{(0)} = \left\langle \psi_1^{(0)} \middle| \frac{e^2}{r_{12}} \middle| \psi_1^{(0)} \right\rangle. \tag{46b}$$

Next, the functions $\psi_i^{(1)}$ are substituted into (46), instead of $\psi_i^{(0)}$ to find the new value $\chi_i^{(1)}$. The former is substituted back to (45) to evaluate $\psi_i^{(2)}$, etc. If this procedure converges, then the system (45) will yield almost identical wave functions, $\psi_i^{(k)} \simeq \psi_i^{(k-1)}$, for some k. These functions will represent the desired one-electron orbitals for (44). The corresponding value $\chi_i^{(k)}$ is known as the *Hartree self-consistent field*. For polyatomic molecules, Eq. (45) is solved with the tight binding method at each iteration step; this updates the values of coefficients in the linear representations, similar to (34).

According to (45) and (46), the physical interpretation of this method is in the assumption that the electron–electron interaction occurs through the averaged field $\chi_i^{(k)}$, and for a given electron, this field is created by the rest of electrons in the system.

The Hartree method does not comply with the Pauli principle. Using the trial function form (43) instead of (44) allows writing a set of equations for the one-electron wave functions to constitute a multi-electron wave function that satisfies the Pauli principle. This function accounts for some additional characteristics of the quantum system, such as the spin variables of the electrons. Such an approach of solving the multi-electron problem is known as the *Hartree–Fock method* [92]. The resultant one-electron equations, as compared to (45), include additional terms of the type $\chi_{ji}\psi_i^{(1)}$, where χ_{ji} is the *exchange integral*

$$\chi_{ji} = \left\langle \psi_j \middle| \frac{e^2}{r_{ij}} \middle| \psi_i \right\rangle. \tag{47}$$

The successive iteration procedure, similar to (45)–(46), yields the modified molecular orbitals for (43), known as the *Hartree–Fock orbitals*. The corresponding values E_i in (45) are called Hartree–Fock orbital energies. The Hartree–Fock approximation has been used successfully for solving a variety of problems in quantum physics and chemistry. A more detailed description of this method can be found in [93].

3.3. Density functional theory

Though the Hartree–Fock calculations provide reliable results, they are computationally expensive and cannot be applied to large systems. Density functional methods provide an alternative route to yield comparable results at a lower expense, allowing the simulation of molecules with hundreds of atoms.

Within the Hartree–Fock method, the consideration begins with an *exact* Hamiltonian, similar to (30), but an *approximate* trial wave function. This wave function is written by combining the readily available one-electron orbitals, according to (43) or (44), and it is next improved by optimizing the one-electron solutions. In contrast, the density functional model starts with a Hamiltonian, relating to an "idealized" many-electron system, for which the exact wave function is readily available. This solution is updated at each iteration step by optimizing the ideal system closer and closer to the real system [85].

The density functional theory was pioneered by Hohenberg and Kohn [94], who showed that the ground state energy of multi-electron system is a unique functional of the electronic-density of the type

$$E = T[\rho(\mathbf{r})] + V_C[\rho(\mathbf{r})] + E_{XC}[\rho(\mathbf{r})], \tag{48}$$

where T and V_C are known functionals corresponding to the kinetic energy of the electrons and the potential energy of electron–nucleus (or electron–ion) and nucleus–nucleus (or ion–ion) Coulomb interactions, respectively. For large multi-electron atoms, only the outer (valence) electrons are usually considered to contribute to the electronic density of interest, while core electrons and the nucleus are treated together as an ion. In this case, the corresponding electron–ion and ion–ion interaction energies are employed for deriving the V_C term.

An advantage of the density functional theory is that, according to Eq. (48), the ground state energy is obtained without involving a multi-electron wave function, in contrast with formula (33). However, a proper form of the exchange-correlation functional E_{XC} for (47) is in quest here, and it varies in different modifications of this method. In the simplest approach, called *local density functional theory* [95], the exchange and correlation energy is determined as an integral of some function of the total electron density,

$$E_{XC} = \int \rho(\mathbf{r})\varepsilon_{XC}[\rho(\mathbf{r})]\,\mathrm{d}\mathbf{r}, \tag{49}$$

where ε_{XC} is the exchange-correlation energy per electron in a homogeneous electron gas of constant density.

For a system of N-electrons, the electron density function is expressed through the modulus of the one-electron *Kohn–Sham orbitals* ψ_i,

$$\rho(\mathbf{r}) = \sum_{i=1}^{N} |\psi_i(\mathbf{r})|^2 = \sum_{i=1}^{N} \psi_i^*(\mathbf{r})\psi_i(\mathbf{r}). \tag{50}$$

The initial guess for ψ_i is obtained from a set of exact basis functions, the plane waves that give the solution to the Schrödinger equation for a free electron, while the participation coefficients are optimised in a way similar to the Hartree–Fock method, as described below. The updated orbitals are found by solving the Kohn–Sham equation,

$$\left[-\frac{\hbar^2}{2m}\Delta - \sum_{\alpha} \frac{e^2}{r_{\alpha i}} + \frac{e^2}{r} + \int \frac{\rho(\mathbf{r})}{|\mathbf{r}-\mathbf{r}'|}\,\mathrm{d}\mathbf{r}' + V_{XC} - E_i \right] \psi_i^{(1)}(\mathbf{r}) = 0, \quad i = 1, 2, \ldots, N. \tag{51}$$

Here, the terms E_i are the Kohn–Sham orbital energies and V_{XC} is the derivative of the exchange-correlation functional (48) with respect to the electron density:

$$V_{XC}[\rho] = \frac{\delta E_{XC}[\rho]}{\delta \rho}. \tag{52}$$

The improved set of Kohn–Sham orbitals, $\psi_i^{(1)}$, is next used to compute a more accurate density function, according to (49). These iterations repeat until the exchange-correlation energy and the density converge to within some tolerance.

The local density functional theory provides a very rough approximation for the molecular system, because it assumes a uniform total electron density throughout the molecular system. Non-local density functional approaches have been also developed to account for variations in the total density, e.g. [96–98]. This is accomplished by introducing a dependence of ground state energy also on the *gradient* of the electron density, besides the density itself.

The original density functional procedure (49)–(52) in general involves $O(N^3)$ order of computation, N is the number of electrons, as compared with $O(N^4)$ for the Hartree–Fock and tight binding methods. Important improvements have been made using the Car–Parrinello MD method [99] and conjugate gradient method [100]. The Car–Parrinello method reduces the order to $O(N^2)$, while the conjugate-gradient method can, as shown in [100], be even more efficient. Standard computer packages are currently available to accomplish ab initio calculations based on the density functional theory; as an example, we mention the VASP code, which was developed at the University of Vienna [101].

4. Limitations of MD simulations

Molecular dynamics (MD) simulations have become a powerful tool for elucidating complex physical phenomena. However, the length and time scales that can be probed using MD are still fairly limited. For

the study of problems such as nanoscale coatings, ion-beam deposition, nanoindentation and stiction in MEMS devices, models need to be on the scale of several microns, consisting of billions of atoms, which is too large for current MD simulations.

The major task of the MD simulation is to predict the time-dependent trajectories in a system of interacting particles. For this purpose, time-integration algorithms were devised to solve the equations of motion (5) based upon truncated Taylor's expansions with respect to time. Detailed descriptions of these simulation algorithms can be found elsewhere [51,52].

Efficiency and accuracy are the two most important criteria guiding the development of simulation methods. Both depend on the complexity of the interatomic potentials and the time-integration algorithms used in the simulation. With the computational power available today, a typical MD simulation domain contains several millions of atoms. Consequently, MD simulations have their own limitations, which will be discussed below in Sections 4.1 and 4.2.

4.1. Effect of boundary conditions

Due to the limitations in computer performance, MD simulations consider only small representative volume elements of the full system under analysis, while the true effect of the surrounding media is typically ignored with the use of rigid or periodic boundary conditions. Therefore, the physical behavior and properties of representative volume elements cannot be unambiguously attributed to a corresponding macro-scale system of interest.

In a small MD system, a large fraction of atoms is located on the surface of the domain. As a result, these surface effects dominate the properties of the simulated material. The use of periodic boundary conditions (PBC) can overcome the surface effects to a certain extent. However, it introduces artificial periodicity into the simulated system. It is thus arguable whether a small simulation box with imposed PBC represents the macroscopic system it intends to simulate.

In general, the effect of PBC depends on the range of the interatomic potentials and the phenomena under investigation. A simulation is considered to be valid only when the size of the simulated domain is larger than the cut-off radius of the interatomic potential and the effective range of the phenomenon under investigation. Consider, for example, the induction of compressive stresses in carbon thin films grown via ion beam deposition [102,103]. The dominant mechanisms responsible for stress formation are defect production and recombination within displacement and thermal spikes induced by energetic carbon neutrals. Such a physical process takes place within a region on the order of 1 nm centered around the impacting carbon neutrals, provided that the impact energy of the carbon neutrals is less than 200 eV. Note that since the carbon-carbon interaction is short-ranged, a valid MD simulation for this case can be based on a substrate with size on the order of 1 nm.

The use of fixed or periodic boundary conditions may not be capable of capturing long-ranged physical processes. For example, in simulating ion-beam deposition, a non-zero Kapitza resistance is generated, which leads to anomalous heating at the boundaries of the molecular model. Waves that are generated in the molecular mechanics domain cannot pass into the surrounding media. Instead, waves are reflected back into the atomistic domain, as shown in Fig. 5a. In reality, the thermal energy in the form of localized lattice vibrations would be dissipated away by phonons. Failure to model these correctly leads to unphysical behavior of the simulated system. The reflected wave interacts with other physical processes, causing pronounced simulation errors, such as bouncing of the deposited ions due to the increase in kinetic energy of the lattice atoms, Fig. 5b. One commonly used technique to avoid spurious wave reflection is to apply fictitious damping forces to several layers of atoms next to the boundaries. However, this method is still ad fhoc and is particularly ineffective for coherent waves.

Another example is the simulation of nanoindentation processes [104–107], Fig. 6. In a nanoindentation experiment, the size of a typical indenter is of the order of tens of nanometers. To minimize the boundary

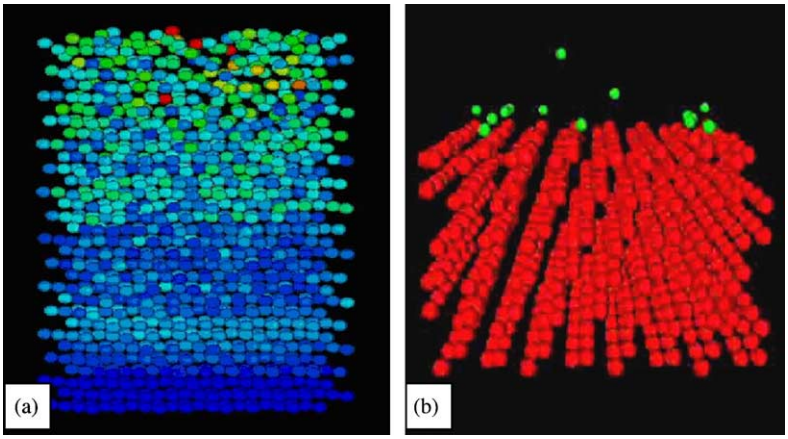

Fig. 5. Ion-beam deposition: (a) waves due to ion–lattice collisions are reflected from the boundaries; (b) the collisions heat up the lattice causing unrealistic bouncing of the deposited ions.

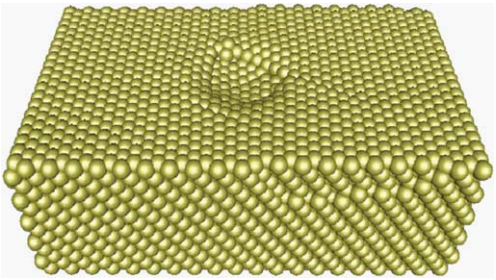

Fig. 6. Indentation pattern in a golden substrate: MD simulation. Actual imprint size can be tens-to-hundreds of nanometers.

effects, the substrate for the MD simulations must be at least an order of magnitude larger than the indenter. A model for this system would easily fall beyond the affordable range of the modern computer power. To reduce the computational requirements, a virtual potential is often introduced to mimic the indenter. The effective domain of this potential is much smaller than that of a real indenter. Rigid boundary conditions are typically applied on the bottom of the substrate with periodic boundary conditions in the indentation plane. These boundary conditions artificially stiffen the material, which suppresses the nucleation of dislocations. Furthermore, the evolution of any emitted dislocations may also be affected by these boundary conditions. The validity of the corresponding force versus indentation depth curve becomes questionable, especially when a small domain is simulated.

Reliability studies of the simulation results require the estimation of PBC effects. However, studies of PBC effects are frequently hampered by the difficulty in isolating the periodicity effects from other effects. A standard approach is to test the simulation results repeatedly with increasing simulation domain sizes.

MD simulations of dynamic fracture have been fairly successful in recent years. However, one potential limitation of using MD only lies in the fact that huge numbers of atoms must be used in the fracture simulations [144,145]. The reason for this is due to the fact that it is crucial in MD fracture simulations to allow waves that have been emitted from the crack tip region to propagate unimpeded away from the crack. If this is not allowed to happen, then the waves reflect from the MD boundaries and continue to incorrectly participate in the crack tip dynamics. Two snapshots of an MD fracture simulation, depicted in Fig. 7,

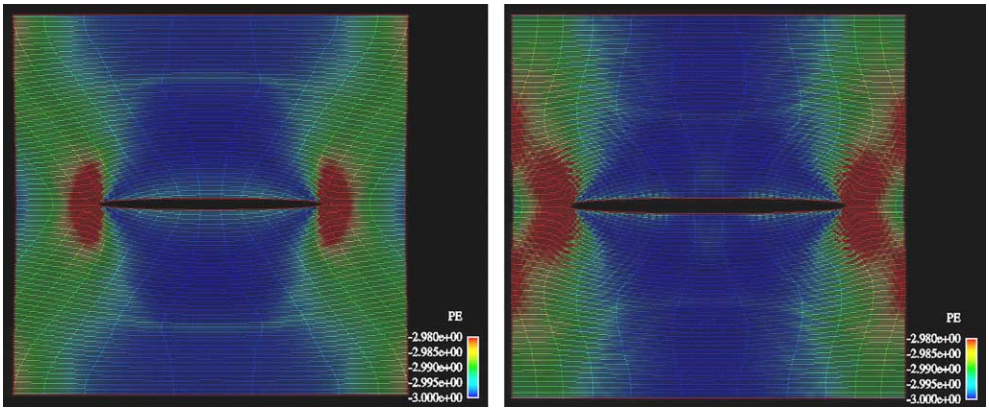

Fig. 7. A potential energy profile for MD fracture simulation: the fracture dynamics is affected by elastic waves, emitted by the crack tip (left) and reflected back by the MD domain boundaries (right).

illustrate this process. The wave created due to opening the fracture surfaces heads out towards the MD boundary, reflects from it, and propagates back in towards the crack. Once the wave hits the crack, it will interfere with the crack dynamics. In this simulation, the wave front is plane and parallel to the crack face.

In order to avoid this spurious interference, MD simulations of fracture must be very large, typically on the order of many millions of atoms, to ensure a domain that is large enough to prevent wave interference at the crack tip. Though the increase in computational power has made million atom MD calculations fairly commonplace, it appears to be computationally and physically unnecessary to have full atomistic resolution far from the crack tip.

Because of the large domain requirement on the MD region, it appears that this type of problem would be well suited to multiple-scale analysis techniques. Another issue which supports this is the fact that the waves emitted from the crack tip are usually elastic in nature, and do not cause atomic imperfections (i.e. dislocations) far from the crack tip. Therefore, we will discuss application of the bridging scale method, a multiple-scale method that will be introduced in detail later in this work, to this problem. The crack propagation can be correctly modeled using full atomistic resolution, while the propagation of the elastic waves away from the crack tip can be accurately modeled and captured using a continuum formulation. The usage of finite elements far from the crack tip would reduce the computational expense of having full atomistic resolution, while still accurately capturing the necessary physics.

4.2. Coupling to an external bath

In MD simulations, it is often required to maintain a certain temperature in the ensemble. For example, in an ion-deposition process, part of the kinetic energy of the impacting ions is transmitted to thermal energy in the form of concentrated lattice vibration. In reality, the thermal energy would be damped away by phonons. However, the use of PBC prohibits the transmission of the thermal energy to the surrounding media. This may result in a spurious growth of the system temperature and consequent evaporation of the surface atoms. Furthermore, studying temperature-dependence macroscopic properties also requires control of the system temperature.

A general method of controlling temperature in a molecular system is to couple the molecular system to an external bath, thereby allowing heat exchange between the system and the external bath [53]. Such a coupling can be accomplished by adding stochastic and friction terms in the equations of motion, yielding a Langevin equation for selected atom i,

$$m_i\dot{\mathbf{v}}_i = \mathbf{F}_i - m_i\gamma_i\mathbf{v}_i + \mathbf{R}, \tag{53}$$

where γ_i is the damping constant that determines the strength of the coupling to the bath, and $\mathbf{R}$ is the Gaussian stochastic variable.

Through the Langevin equation, the system not only globally couples to the external bath, but is also subjected to random noise. In the case where the global coupling is the only interest, the coupling can be established by

$$m_i\dot{\mathbf{v}}_i = \mathbf{F}_i + m_i\gamma\left(\frac{T_0}{T} - 1\right)\mathbf{v}_i, \tag{54}$$

where T_0 is the reference temperature, and T is the kinetic temperature of the system. Note that in Eq. (54), the friction constants for all the selected atoms are equal, i.e., $\gamma_i = \gamma$. Effectively, this coupling proportionally scales the velocity by a factor of λ per time step, with $\lambda = 1 + \gamma\Delta t(T_0/T - 1)$. Eq. (54) shows that the exchange of thermal energy between the external bath and the system is solely based on their temperature difference. When $T_0 < T$, thermal energy is dissipated away into the external bath; when $T_0 > T$, the system absorbs energy from the external bath.

Another issue lies in choosing the magnitude of the damping constant. On the one hand, the damping constant must be large enough such that energy can be removed efficiently from the atoms without causing substantial temperature change. On the other, it should be small enough that the trajectories of individual particles are not perturbed too strongly by the coupling.

In the study of nanotribology [108,109], it is of great interest in evaluating the dissipated energy by friction from the simulated ensemble and the external bath. The above analysis shows that the dissipated energy per step can be written as

$$E_d = \sum_i \mathbf{f}_i^{\text{damp}} \cdot \mathbf{v}_i\Delta t, \tag{55}$$

where $\mathbf{f}_i^{\text{damp}} = m_i\gamma(T_0/T - 1)\mathbf{v}_i$ is the damping force for atom i. The index i runs over all the atoms that are coupled to the external bath for each time step. The average frictional force can be computed from the accumulated energy dissipation and the sliding distance. Equivalently, one can calculate the frictional forces through the discrete summation of the atomic force, as shown in Fig. 8.

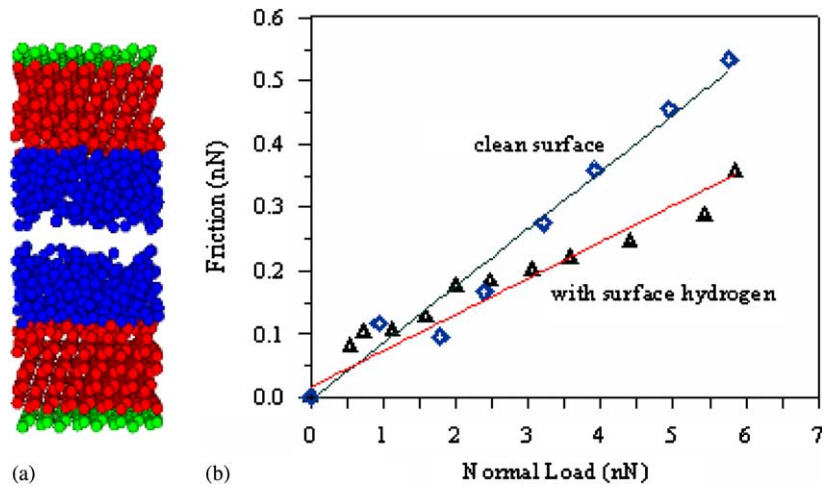

Fig. 8. Friction behavior of a hydrocarbon system [109]: (a) simulation model of friction between two molecular surfaces; (b) comparison of the friction coefficients for hydrogen-terminated carbon surfaces and clean carbon surfaces.

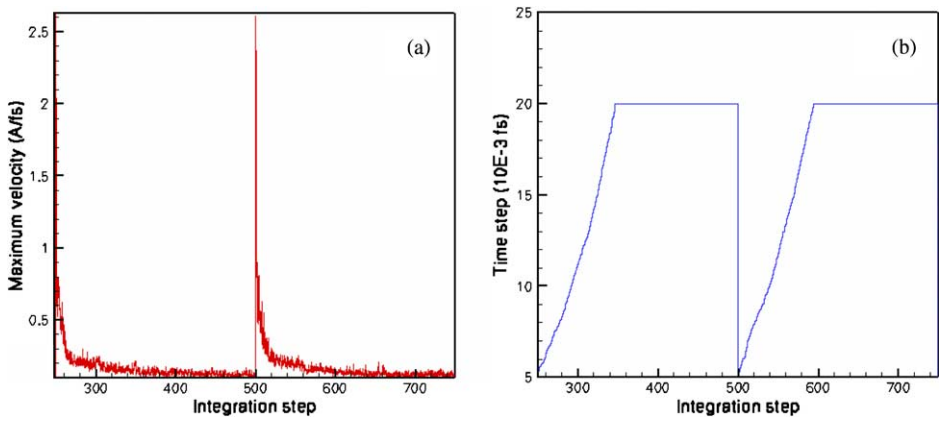

Fig. 9. Using varying time-step in the simulation of ion-beam deposition. (a) Maximum velocity of atoms in the system. The peaks correspond to the deposition of an energetic ion. (b) Time step in the simulation based on the maximum velocity profile.

Thermal coupling virtually mimics the heat exchange between the domain under investigation and its surrounding medium. Representing the underlying physical process by simply applying an artificial friction force to selected Langevin atoms may not be sufficient. Unfortunately, no advanced replacement of this coupling technique is currently available. This weakness motivates the usage of multi-scale simulations in which the bulk material that surrounds the MD domain is allowed to influence the energetics of the MD domain. This topic will be addressed in Section 5.

4.3. Time step

In MD simulations, the time step is one of the crucial parameters that determines computational expense. Two criteria must be followed in choosing the value of the time step. First, the time step should be small enough so that the trajectory of each atom is realistic. Note that the truncation error in a simulation is power-law proportional to the time step. A large time step would lead to divergent physical behavior. Secondly, the time step should be large enough so that the simulation is efficient.

A constant time step is commonly implemented in MD simulations for the simplicity of the algorithm. In the case of simulating large time-scale phenomena, using a constant time-step would require tremendous power. In a dynamic process, where the maximum atom velocity varies, a varying time step can be used to improve the efficiency of the simulation. Specifically, it can be chosen inversely proportional to the maximum velocity of particles in the ensemble. One way to assign a time step for the next integration step, $(\Delta t)_{n+1}$, is to account for the maximum atomic velocities on two successive steps, as

$$\Delta t_{n+1} = \begin{cases} \Delta t_n \left(1 + \alpha \left(V_n^{\max} - V_{n+1}^{\max}\right)/V_{n+1}^{\max}\right) & V_{n+1}^{\max} \leqslant V_n^{\max}, \\ \Delta t^{\max} & V_{n+1}^{\max} > V_n^{\max}, \end{cases} \tag{56}$$

where α is the time-step increment parameter. Note that the truncation error is proportional to the time step, a maximum time step is chosen in Eq. (56). This varying time-step strategy has been used in simulating the ion-beam deposition process; see Fig. 9. It is found that the efficiency of simulations can be markedly improved without considerably affecting the simulation results.

5. Multi-scale simulation methods

Over the past few decades, continuum methods have dominated materials modeling research. This approach of predicting material deformation and failure by implicitly averaging atomic scale dynamics and

defect evolution over time and space, however, is valid only for large enough systems that include a substantial number of defects. As a result, numerous experimental observations of material behavior cannot be readily explained within the continuum mechanics framework: dislocation patterns in fatigue and creep, surface roughening and crack nucleation in fatigue, the inherent inhomogeneity of plastic deformation, the statistical nature of brittle failure, plastic flow localization in shear bands, and the effects of size, geometry, and stress state on yield properties. Thus, there is a considerable effort to find fundamental descriptions for strength and failure properties of nanoscale materials, taking into account their atomic structures. The use of MD simulations has provided useful information of chemical interactions at the nanoscale. However, MD simulations have their own limitations, as discussed in the previous section. Typical atomistic simulations are still restricted to very small systems consisting of several million atoms or less and timescales on the order of picoseconds. Thus, even for nanoscale structures and materials, atomistic modeling would be computationally prohibitive.

The limitations of atomistic simulations and continuum mechanics, along with practical needs arising from the heterogeneous nature of engineering materials, have motivated research on multi-scale simulations that bridge atomistic simulations and continuum modeling [110–117,125–132]. In order to make the computations tractable, multi-scale models generally make use of a coarse-fine decomposition. An atomistic simulation method, such as MD, is used in a small subregion of the domain in which it is crucial to capture the individual atomistic dynamics accurately. A continuum simulation is used in all other regions of the domain in which the deformation is considered to be homogeneous and smooth. Since the continuum region is usually chosen to be much larger than the atomistic region, the overall domain of interest can be considerably large. A purely atomistic solution is normally not affordable on this domain, though the multi-scale solution would presumably provide the detailed atomistic information only when and where it is necessary. The key issue is then the coupling between the coarse and fine scales. Depending on the method of information exchange between the coarse and fine regions, multi-scale methods can be classified into three groups: hierarchical, concurrent, and multi-scale boundary conditions.

Hierarchical approaches (Section 5.1) embed the intrinsic atomistic properties of the solid in the continuum formulation according to the Cauchy–Born rule, so that small scales depend on large scales in some predictable way. Hierarchical techniques are based on the assumption of homogeneous lattice deformation; therefore they are more effective for elastic single-phase problems. Difficulties typically arise from modeling defects in atomic lattices, dislocations, and failure phenomena.

Within *concurrent* methods (Sections 5.2, 5.3 and 5.5), the behavior at each length scale depends strongly on the others. An appropriate model is solved at each length scale simultaneously (continuum mechanics for macro-elastic media, molecular dynamics for large groups of atoms and quantum mechanics for bond breaking), while a smooth coupling is introduced between the different scales. The interscale dependence is complicated, and it is not pre-assigned. Concurrent approaches are more relevant for studying complicated problems, involving inhomogeneous lattice deformation, fracture in multi-phase macroscopic materials, and nanofluidics. However, two arguable issues do typically arise: (a) how to separate the scales, and (b) what is the adequate mechanism of coupling the atomistic and continuum simulations.

Multi-scale boundary conditions for molecular dynamic simulations (Section 5.4) is an emerging approach not to involve the explicit continuum model, so that the issues of separating the scales and coupling the simulations do not arise. In this case, the coarse grain behavior is taken into account on the fine/coarse grain interface at the atomistic level through the lattice impedance techniques. These methods, though, may appear to be more effective than the concurrent methods only for a particular class of problems with linear coarse grains in solids. Alternatively, the multi-scale boundary conditions are employed within concurrent coupling methods to represent atomistic behavior in the continuum domain. That results in a smooth FE/MD coupling, without involving an artificial handshake region at the atomistic/continuum interface and a dense FE mesh scaled down the chemical bond lengths.

5.1. Hierarchical modelling of heterogeneous materials

The heterogeneous nature of engineering materials calls for a multi-field decomposition technique in modeling material deformation and failure [110–128]. Within the framework of continuum mechanics, a multi-field decomposition takes the localized deformation of materials into account by including a high-order term in the constitutive relation [125]. A general idea of this technique is to decompose the deformation field into macro- and micro-components,

$$\mathbf{u}(\bar{\mathbf{x}}+\mathbf{y}) = \mathbf{u}(\bar{\mathbf{x}}) + \mathbf{u}_m(\bar{\mathbf{x}}+\mathbf{y}), \tag{57}$$

where $\mathbf{u}(\bar{\mathbf{x}}+\mathbf{y})$ is the total displacement field, $\mathbf{u}(\bar{\mathbf{x}})$ is the displacement at the center of the micro-scale cell, and $\mathbf{u}_m(\bar{\mathbf{x}}+\mathbf{y})$ is the relative displacement to the center of the micro-cell. This displacement field decomposition leads to the following form of system potential energy:

$$W = \int_{\Omega_x} (\sigma_{ij}\varepsilon_{ij} + \sigma'_{ij}(\chi_{ij} - F_{ij}) + \tau_{kji}\chi_{ij,k})\,\mathrm{d}\Omega + \int_{\Omega_x} (b_i u_i + B_{ij}\chi_{ij})\,\mathrm{d}\Omega + \int_{\Gamma_x} (t_i u_i + T_{ij}\chi_{ij})\,\mathrm{d}\Gamma, \tag{58}$$

where σ_{ij}, σ'_{ij} and τ_{kji} the macro-stress, micro-stress and the second micro-stress tensors, respectively, F_{ij} and χ_{ij} are the macro- and micro-deformation gradients, ε_{ij} is the symmetric part of F_{ij}, Ω_x is the volume of the computational domain, Γ_x is the boundary of the domain Ω_x, b_i and B_{ij} are the body force and the body couple, and t_i and T_{ij} are the applied force and moment on the boundary, respectively. The principle of virtual work leads to following point-wise governing equations in terms of the macro-scale and the micro-field deformation gradient, as

$$(\sigma_{ij} - \sigma'_{ij})_{,j} = b_i, \quad \sigma'_{ij} - \tau_{kji,k} = B_{ij} \quad \text{in } \Omega_x, \tag{59a}$$

$$(\sigma_{ij} - \sigma'_{ij})n_j = t_i, \quad \tau_{kji}n_k = T_{ij} \quad \text{on } \Gamma_x, \tag{59b}$$

where n_j is the normal at the boundary. Differing from the conventional continuum mechanics formulation, the equilibrium condition here consists of both the force and couple balance in the domain and on the boundary, respectively.

In order to solve the boundary value problem described by (59), the constitutive laws at different scales must be established. The heterogeneous nature of the materials under investigation suggests a hierarchical modeling technique. A general feature of hierarchical methods is that simulations at different length scales are performed separately. The coupling between scales is realized by embedding the information gained from the fine-scale simulation into the coarser scale simulation.

A hierarchical model has been proposed for quantum design of Cybersteel that contains particles on different length scales [126], as shown in Fig. 10. The primary inclusions, which improve the yielding strength of the material, are on the order of 1 μm; the secondary particles, which enhance the ductility of the material, are on the order of 0.1 μm. The failure of the Cybersteel involves particle–matrix interface debonding, void nucleation and growth, shear localization and ductile fracture. These failure phenomena occur on different length scales: the particle–matrix interface debonding takes place on the quantum scale, void nucleation and growth on the sub-micron scale, shear localization on the micro scale and fracture on the macroscopic scale. In order to establish a reliable macroscopic constitutive equation for the Cybersteel, computational tools are needed to bridge the physics at different length scales hierarchically. The objective of quantum steel design is to use these computational tools in the multi-physics based design of high-strength and high-toughness steels for naval applications.

Fig. 10 presents a bottom-up multi-scale strategy for modeling the macroscopic fracture of the Cybersteel. Starting from the quantum scale, the particle–matrix interface decohesion is characterized by a first-principles based traction-separation law, which is embedded into the simulation of the submicro-cell that contains secondary particles. This procedure is repeated hierarchically for the micro-cell that contains the

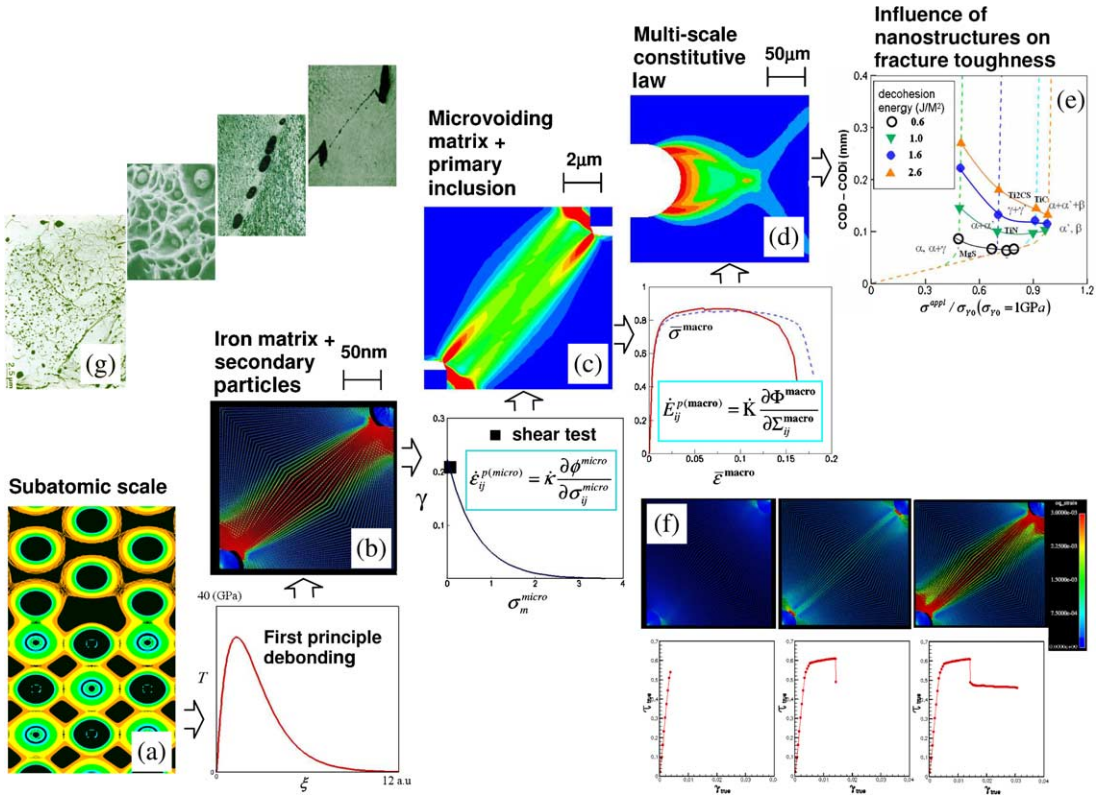

Fig. 10. Hierarchical modeling of Cybersteel [126]: (a) Quantum mechanics calculations yield the traction-separation law. (b) Concurrent modeling of the submicro-cell with embedded traction-separation law. (c) Concurrent modeling of the micro-cell with embedded constitutive law of the submicro-cell. (d) Modeling the fracture of the Cybersteel with embedded constitutive law of the micro-cell. (e) Fracture toughness and yield strength of the Cybersteel as a function of decohesion energy, determined by geometry of the nanostructures. (f) Snap-shots of the localization induced debonding process. (g) Experimental observations.

primary inclusions to establish the macroscopic constitutive law that is in turn used to simulate the macroscopic fracture of the Cybersteel. Detailed descriptions of the computational strategy at different length scales are presented as follows.

(I) *Quantum scale*: The interfacial traction-separation law of the inclusion-matrix is established based on first-principles calculations (Fig. 10a). The traction-separation law is determined by the material composition of both the particles and the matrix. Key parameters that characterize the traction-separation law are determined, such as the peak force, the critical separation at which the traction vanishes, and the interface binding energy. As the interfacial cohesive law serves as a fundamental governing equation that ultimately determines the mechanical properties of the bulk materials, these key parameters are regarded as design parameters for the Cybersteel.

(II) *Submicro-scale*: Within the framework of energy conservation, the first principles-based interfacial traction-separation law is embedded into the modeling of the constitutive law for the submicro-cell (Fig. 10b). The particle–matrix debonding process is modeled by employing a concurrent method. Specifically, the particles and the matrix are modeled by finite elements, while the interface is modeled by molecular dynamics. The deformation behavior, typically characterized by interface debonding induced void nucleation and growth, is determined by not only the key parameters associated with the traction-separation law,

but also the volume fraction, orientation and distribution of the secondary particles. A comprehensive modeling at various loading conditions gives rise to a constitutive law of the submicro-cell that takes into account all the abovementioned effects, as

$$\boldsymbol{\Sigma}_m = \boldsymbol{\Phi}_m(\boldsymbol{\Xi}_m, \boldsymbol{\eta}_{\text{T-S}}, \boldsymbol{\eta}_{\text{SP}}), \tag{60}$$

where $\boldsymbol{\eta}_{\text{T-S}}$ represents all the key parameters of the first-principles based traction-separation law of the interface, while $\boldsymbol{\eta}_{\text{SP}}$ represents the parameters that are associated with the secondary particles. $\boldsymbol{\Sigma}_m$ and $\boldsymbol{\Xi}_m$ are the average stress and strain of the submicro-cell, respectively, and defined as

$$\boldsymbol{\Sigma}_m = \frac{1}{V_m}\int_{V_m} \boldsymbol{\sigma}_m \,\mathrm{d}V, \tag{61a}$$

$$\boldsymbol{\Xi}_m = \frac{1}{V_m}\int_{V_m} \mathbf{E}_m \,\mathrm{d}V. \tag{61b}$$

Note that both the Cauchy stress $\boldsymbol{\sigma}_m$ and the normal strain $\mathbf{E}_m$ are defined within the framework of continuum mechanics.

Besides the constitutive law, a plastic flow rule of the submicro-cell can be established by a series of shear tests of the cell.

(III) *Micro-scale*: The constitutive relation and the plastic flow rule established for the submicro-cell, in conjunction with the first-principles based traction-separation law for interfacial decohesion, are incorporated into the modeling of the deformation of the micro-cell (Fig. 10c). A similar concurrent method can be employed for the modeling. Based on the simulation results, the constitutive law of the micro-cell, along with the plastic flow rule can be established similarly as for submicro-cell. For simplicity, the constitutive law of the micro-cell is written as

$$\boldsymbol{\Sigma}_{\text{e}} = \boldsymbol{\Phi}_{\text{e}}(\boldsymbol{\Xi}_{\text{e}}, \boldsymbol{\eta}), \tag{62}$$

where $\boldsymbol{\eta}$ includes not only the parameters that are inherited from the submicro-cell, but also those associated with the primary inclusions. $\boldsymbol{\Sigma}_{\text{e}}$ and $\boldsymbol{\Xi}_{\text{e}}$ are the averages of the Cauchy stress and normal strain of the micro-cell, respectively. An associated plastic flow rule is also established through the simulation.

(IV) *Macro-scale*: The constitutive law established for the micro-cell is considered as the macroscopic constitutive relations of the Cybersteel with which problems such as fracture and damage can are simulated using multi-field decomposition methods (Fig. 10d). The macroscopic properties, such as fracture toughness, frequently represented by the crack opening displacement (COD), and strength of the steel can be obtained (Fig. 10e).

The hierarchical modeling described above establishes a direct relationship between the macroscopic properties and the key nanoscale parameters, which provides guidelines for both the development of improved material fabrication processes as well as helping to facilitate the mechanical design of the material. Thus, the final results, as shown in Fig. 10, serves as a design curve from which optimal nanoscale parameters can be determined for specified macroscopic properties. Given an experimentally established relationship between the fabrication process and the interfacial traction-separation law, the design curve can be further used to optimize fabrication conditions of the material.

The multi-field decomposition technique combined with the hierarchical modeling described above is general and applicable to other heterogeneous materials. However, this integrated method suffers its own limitations: the study of the material response in the fine scale may not be complete, or it may not be possible to explicitly include all the information of the material behavior in one scale and pass it to another scale without information loss. These problems become more pronounced when the field is decomposed into more than two length scales.

5.2. Concurrent methods

To avoid information loss when passing information from one length scale to another, researchers have expended a great deal of effort in developing concurrent methods to achieve a seamless bridging between different length scales. In a concurrent method, simulations at different length scales are performed *simultaneously* and the information interfaces between different length scales continually transmit information from one simulation to the other. In the following, three representative concurrent methods are briefly presented.

5.2.1. MAAD

MAAD was developed by Abraham, Broughton and co-workers [110,111] and named after the computation at three different length scales: macroscopic, atomistic, and ab initio dynamics. In this method, three different computational methods, namely tight-binding (TB), molecular dynamics (MD) and finite-element (FE) are concurrently linked together to simulate crack propagation in a brittle solid. Tight binding is used to simulate the atomic bond breaking right at the crack-tip; molecular dynamics at the region around the crack-tip; finite elements are used in the region far from the crack-tip where the deformation field is generally smooth. The dynamics of the entire system is governed by a total Hamiltonian function that combines the separate Hamiltonians of the three different regions. In this method, the finite-element mesh is graded down to the lattice size. While MAAD has been successfully applied to brittle fracture in Silicon, two major issues remain. The first is that all three equations of motion (TB, MD and FE) are integrated forward in time using the same timestep, i.e. the smallest, or TB timestep. Because of this, many timesteps are wasted in updating the MD and FE equations of motion, as the timescales governing those simulations are orders of magnitude larger. The second lingering issue lies in the coupling of the differing simulations. In MAAD, the coupling is accomplished by assuming in the transition region that each simulation contributes an equal amount of energy to the total energy. However, no rigorous studies have been performed to quantify the effectiveness of this method in eliminating spurious wave reflection at the simulation boundaries.

5.2.2. Quasi-continuum method

Another method developed recently is the quasi-continuum (QC) method [113–117]. In this method, the continuum framework and continuum particle concept are retained, while the macroscopic constitutive law is replaced by that from direct atomistic calculations. Each continuum particle is regarded as a small crystallite surrounding a representative atom. The strain energy associated with the representative atom can be computed by summing up the interatomic potential of the crystallite following the Cauchy–Born rule. The fundamentals of this method are presented below.

Under an applied external stress/strain, the material under investigation undergoes a motion described by a deformation map ψ from the initial, undeformed configuration to the current, deformed configuration. For quasi-static analysis, the equilibrium conditions are obtained by minimizing the total potential energy of the system

$$\Pi(\psi) = W^{\text{int}}(\psi) - W^{\text{ext}}(\psi), \tag{63}$$

where $\Pi(\psi)$ is the total potential energy of the system, $W^{\text{int}}(\psi) = \int_{V_0} w(\psi)\,\mathrm{d}V$ is the internal energy, $W^{\text{ext}}(\psi)$ is the external energy and $w(\psi)$ is the strain-energy density. In finite element calculations, the integration can be conveniently performed by numerical quadrature at the continuum level, as

$$\int_{V_0} w(\psi)\,\mathrm{d}V = \sum_{e=1}^{M}\sum_{q=1}^{Q} \lambda_q^e w[\psi(\xi_q^e)], \tag{64}$$

where M is the total element number in the finite-element calculation, Q is the order of the quadrature rule, λ_q^e and ξ_q^e are the quadrature weights and points for element e.

The multi-scale concept is brought into picture in computing the strain-energy at quadrature points. In the local QC method, each continuum point in the solid is represented locally by an infinite crystal subjected to homogeneous deformation.

The energetics of a continuum can be connected to that of the underlying atoms through the *Cauchy–Born rule*, which hypothesizes that the infinite crystal underlying each continuum particle deforms according to a locally uniform, continuum deformation gradient. Therefore, the strain-energy density at a continuum point can be approximated by an atomistic model. In a Bravais lattice, lattice vectors deform by a deformation gradient $\mathbf{F}$,

$$\mathbf{r} = \mathbf{F}\mathbf{r}^0, \tag{65}$$

where $\mathbf{r}^0$ and $\mathbf{r}$ are the lattice vectors at the reference and current, deformed configuration, respectively. Due to the periodicity of the Bravais lattice, the strain energy per atom can be written as

$$\Lambda = \frac{1}{2}\sum_j V(r^j), \tag{66}$$

where V is the potential between the atom and its neighboring atoms, r^j is the spatial distance between the atom and the atom j that is located within a prescribed cut-off radius. Note that the strain energy per unit reference volume, w, is related to the energy per atom Λ by $w = \Lambda/\Omega_0$, where Ω_0 is the volume of the reference unit cell.

By placing in correspondence the deformation of a continuum particle and the underlying crystal at the atomic scale, traditional continuum measures of stress and material modulus can be directly computed from the same atomistic model. For example, the Cauchy stress at the current configuration is obtained as

$$\boldsymbol{\sigma} = \frac{1}{2\Omega}\sum_j \frac{\partial V}{\partial r^j}\frac{\mathbf{r}^j \otimes \mathbf{r}^j}{r^j}, \tag{67}$$

where Ω is the volume of the current unit cell. The above expressions are of a local QC formulation. Because of the homogeneous deformation restriction that the Cauchy–Born rules enforces upon the underlying atomistic system, a non-local QC formulation [118] was developed, which allows atomistic defects such as dislocations to occur. Furthermore, a finite-temperature quasi-continuum model has been developed, as shown in the Ref. [119].

The QC method has been used in simulation of dislocation motion, interactions among grain boundaries, nanoindentation and fracture. Complications of this method are introduced by requiring the continuum mesh to be graded down to the scale of the atomic lattice in regions of localized deformation. A more detailed review on the quasi-continuum and related methods can be found in [120].

5.3. Bridging scale method

In overcoming the requirement of grading finite-element mesh down to the lattice size, as in QC and MAAD methods, a concurrent coupling method has been recently developed by Liu and co-workers [57,58,125, 127–130]. A unique characteristic of this method is that it is formally assumed that the FE and MD solutions exist *simultaneously* in the entire computational domain and MD calculations are performed only in the regions that are necessary. The basic idea is to decompose the total displacement field $\mathbf{u}(\mathbf{x})$ into coarse and fine scales

$$\mathbf{u}(\mathbf{x}, t) = \bar{\mathbf{u}}(\mathbf{x}, t) + \mathbf{u}'(\mathbf{x}, t), \tag{68}$$

where $\bar{\mathbf{u}}(\mathbf{x},t)$ is the coarse-scale solution and $\mathbf{u}'(\mathbf{x},t)$ is the fine-scale solution, corresponding to the part that has a vanishing projection onto the coarse scale basis functions. The coarse scale solution can be interpolated by basic finite-element shape functions as $\bar{\mathbf{u}} = \mathbf{N}\mathbf{d}$, where $\mathbf{d}$ is the FE solution and $\mathbf{N}$ is the shape function evaluated at atomic locations. Wagner and Liu [129] demonstrated that $\mathbf{u}' = \mathbf{Q}\mathbf{q}$, where $\mathbf{q}$ is the MD solution, $\mathbf{Q} = \mathbf{I} - \mathbf{P}$, $\mathbf{P}$ is a projection operator that depends on both shape functions and the properties of the atomic lattice, and $\mathbf{I}$ is the identity matrix.

5.3.1. Quasi-static problems

Within the bridging scale method, the governing equations are obtained by employing the principle of virtual work to give

$$\mathbf{N}^{\mathrm{T}}\mathbf{f}^{\mathrm{int}}(\mathbf{d},\mathbf{q}) = \mathbf{N}^{\mathrm{T}}\mathbf{f}^{\mathrm{ext}}(\mathbf{d},\mathbf{q}), \tag{69a}$$

$$\mathbf{Q}^{\mathrm{T}}\mathbf{f}^{\mathrm{int}}(\mathbf{d},\mathbf{q}) = \mathbf{Q}^{\mathrm{T}}\mathbf{f}^{\mathrm{ext}}(\mathbf{d},\mathbf{q}), \tag{69b}$$

where $\mathbf{f}^{\mathrm{int}} = -\partial U(\mathbf{u})/\partial\mathbf{u}$ is the internal force, and $\mathbf{f}^{\mathrm{ext}}$ is the external force. The first equation is solved over the entire domain, while the solution of the second equation in (69) is equivalent to that from MD simulation, and is hence only solved in localized region. Note that these two Eq. (69) are coupled. A Newton's method can be used to iteratively solve the coupled equations. Bridging between the coarse and fine scale is realized by transparently exchanging information between coarse and fine scale regions.

It remains to be shown how the internal forces are calculated for the coarse scale simulation. Note that the energy density associated with α is directly related to the bond vector over an effective domain, ΔV_α in the deformed configuration. The total potential energy in the system can be written as a discrete summation over all the atoms: the coarse scale simulation provides boundary conditions for the fine scale simulation, while the fine scale simulation provides an accurate approximation of the internal force that enriches the coarse scale:

$$U = \sum_{\alpha}\sum_{\beta\neq\alpha} w(\mathbf{r}_{\alpha\beta})\Delta V_\alpha, \tag{70}$$

where β runs over all the neighbors of atom α within a prescribed cut-off radius, and w is an energy density function. In the coarse scale, the atomic bond vector is deformed according to the coarse scale deformation field. Thus it can be interpolated by the nodal displacement $\mathbf{d}$. By definition, $\mathbf{N}\mathbf{f}^{\mathrm{int}} = \partial w(\mathbf{r}_{\alpha\beta})/\partial\mathbf{d}$, one has

$$\mathbf{N}\mathbf{f}^{\mathrm{int}} = \sum_{\alpha}\sum_{\beta\neq\alpha} \frac{\partial w(\mathbf{r}_{\alpha\beta})}{\partial\mathbf{r}_{\alpha\beta}}[\mathbf{N}(\mathbf{X}_\beta) - \mathbf{N}(\mathbf{X}_\alpha)]\Delta V_\alpha. \tag{71}$$

The discrete summation of the right-hand side of the above equation makes the evaluation computationally intensive. In practice, the strain energy can be considered as a smooth function. Thus, the discrete summation over the atoms in Eq. (71) can be replaced by evaluations at quadrature points, as

$$\mathbf{N}\mathbf{f}^{\mathrm{int}} = \sum_{\bar{\alpha}}\sum_{\bar{\beta}\neq\bar{\alpha}} \lambda_{\bar{\alpha}}\frac{\partial w(\mathbf{r}_{\bar{\alpha}\bar{\beta}})}{\partial\mathbf{r}_{\bar{\alpha}\bar{\beta}}}[\mathbf{N}(\mathbf{X}_{\bar{\beta}}) - \mathbf{N}(\mathbf{X}_{\bar{\alpha}})]. \tag{72}$$

The advantages of the bridging scale method over other concurrent methods are the following. First, it does not involve the calculation of any high-order tensors, such as the Piola-Kirchoff stress, which makes it computationally more efficient. Secondly, no mesh gradation is required. Finally, the bridging scale method can be extended to the dynamic case [128,129], as outlined in Section 5.3.2, while the quasi-continuum method has currently been shown only for quasi-static processes. All these factors have made the bridging scale method an increasingly popular approach to simulating nanostructured materials.

The bridging scale method has been successfully used in modeling buckling of multi-walled carbon nanotubes [127]. In these simulations, a 15-walled Carbon nanotube (CNT) is considered with the outermost shell being a $(140, 140)$ nanotube, and all inner shells of the (n, n) type; from the outer most shell, n reduces by 5 every layer. The length of the tube is 90 nm and the original MD system contains about 3 million atoms. This is replaced with a system of 27,450 particles. In addition to the particles, two sections along the tube are enriched with molecular structures of multi-walled nanotubes. The position of the enrichment region is determined by a multi-resolution analysis of the coarse scale simulation. Therefore, the scheme is adaptive. The length of each enrichment region is 3.6 nm. Each section contains 49,400 atoms and this adds 296,400 more atomic degrees of freedom. A bending angle with increment of 0.25 degree/step is imposed on both ends of the tube for a total of 100 steps. The multi-scale configuration is illustrated in Fig. 11a. Fig. 11b shows the buckling pattern approximated by meshfree approximation at the final stage of loading, followed by the energy density contour plot for each layer of CNT. Two distinctive buckling patterns can be seen from the meshfree approximation, while the contour plot shows clearly the strain energy concentration at the buckling point. A unique advantage of using the multi-scale method is that we are able to reveal the details of the molecular structure at the kinks, which cannot be resolved by the coarse scale representation alone. The atomic structure of the buckling region for each layer of multi-walled CNT are plotted on the right-hand side of Fig. 11b.

5.3.2. Dynamic simulations

The dynamic formulation for the bridging scale method is obtained according to the Lagrangian formalism. Importantly, the decomposition (68) leads to a Lagrangian of the system in which the kinetic energies of the two scales are uncoupled [129]:

$$L = \tfrac{1}{2}\dot{\mathbf{d}}^{\mathrm{T}}\mathbf{M}\dot{\mathbf{d}} + \tfrac{1}{2}\dot{\mathbf{q}}^{\mathrm{T}}\mathbf{A}\dot{\mathbf{q}} - U(\mathbf{u}), \quad \mathbf{A} = \mathbf{Q}^{\mathrm{T}}\mathbf{M}_{\mathrm{A}}\mathbf{Q}. \tag{73}$$

This in turn provides a convenient form of force coupling between the coarse and fine scale equations of motion:

$$\begin{aligned} \mathbf{M}_{\mathrm{A}}^{\mathrm{f}}\ddot{\mathbf{q}}^{\mathrm{f}} &= \mathbf{f}^{\mathrm{f}}(\mathbf{u}), \\ \mathbf{M}\ddot{\mathbf{d}} &= \mathbf{N}^{\mathrm{T}}\mathbf{f}(\mathbf{u}), \end{aligned} \tag{74}$$

where $\mathbf{M}$ and $\mathbf{M}_{\mathrm{A}}$ are the FE and MD mass matrices, respectively. This form of the equations of motion formally implies that the atomistic MD and continuum FE solutions $\mathbf{q}$ and $\mathbf{d}$ exist simultaneously and

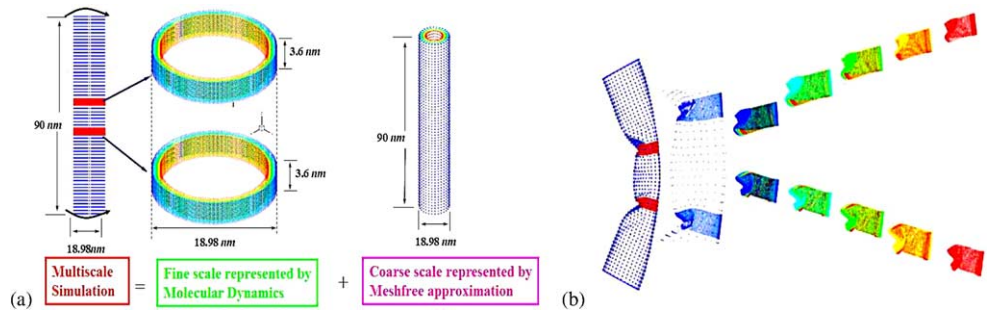

Fig. 11. Multi-scale analysis of a 15-walled CNT by a bridging scale method: (a) The multi-scale simulation model consists of 10 rings of carbon atoms (with 49,400 atoms each) and a meshfree continuum approximation of the 15-walled CNT by 27,450 nodes. (b) The global buckling pattern captured by meshfree method whereas the detailed local buckling of the ten rings of atoms are captured by a concurrent bridging scale molecular dynamic simulation.

everywhere in the computational domain; the upper script index "f" in the first equation stands for the full MD displacement and force vectors, and the atomic mass matrix. This concept is illustrated in Fig. 12.

From the practical point of view, the explicit Lagrangian formulation (74a) is of little merit, because it requires solving the MD equations throughout the continuum; that is in most cases not affordable computationally. Therefore, it is next assumed that the atomistic processes of interest are localized on a small region that features large amplitudes of the relative atomic motion (the fine scale). The rest of the domain (the coarse scale) displays mostly group harmonic character of the atomic motion, so that the corresponding continuum model behaves more or less homogeneously. The atomistic degrees of freedom within the coarse scale are then eliminated from the formulation, and their cumulative effect upon the boundary atoms in the fine scale is taken into account through the impedance force, $\mathbf{f}^{\mathrm{imp}}$, incorporated into the right-hand side of the reduced system of MD equations of motion:

$$\begin{aligned} &\mathbf{M}_{\mathrm{A}}\ddot{\mathbf{q}} = \mathbf{f}(\mathbf{u}) + \mathbf{f}^{\mathrm{imp}}, \\ &\mathbf{M}\ddot{\mathbf{d}} = \mathbf{N}^{\mathrm{T}}\mathbf{f}(\mathbf{u}). \end{aligned} \tag{75a}$$

Here, the MD equation, as compared with (74), involves reduced force and displacement vectors and the mass matrix.

The structure of impedance force resembles the generalized Langevin equation [133,134],

$$\mathbf{f}^{\mathrm{imp}}(t) = \int_0^t \mathbf{\Theta}(t-\tau)(\mathbf{q}(\tau) - \bar{\mathbf{u}}(\tau))\,\mathrm{d}\tau + \mathbf{R}(t), \tag{75b}$$

where $\mathbf{\Theta}$ is a memory kernel function that describes renormalization of the atomic interaction along the boundary of reduced MD domain, and $\mathbf{R}$ is a random function that accounts for thermal atomic motion in the coarse scale. Importantly, the impedance force for the bridging scale formulation is obtained by utilizing the multi-scale boundary conditions for lattice structures (81b); therefore it involves analytically exact structural response at the atomistic level. This is a distinctive feature of the present method, as compared with the "ghost" atom technique to provide the interface displacements and forces based on the FE shape function interpolation.

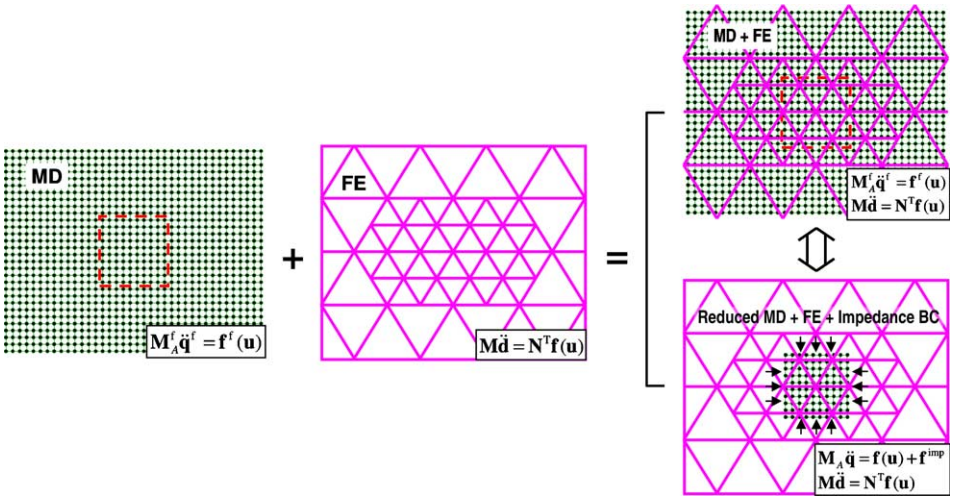

Fig. 12. Illustration of the bridging scale approach: the MD and FE solutions are coupled through the projection technique. The ubiquitous atomistic resolution is replaced with a reduced MD region by utilizing the impedance boundary conditions. The dashed red line shows boundary of the domain of interest.

According to (75b), the physical nature of the force (75b) is due to inertia of the atomic lattice and thermal effects outside the MD domain. The coupled system of Eq. (75) can be solved using existing FE and MD codes along with suitable techniques for exchanging information about the internal forces. The kernel $\mathbf{\Theta}$ function can also be viewed as a lattice impedance matrix, since it encapsulates the impedance of the atomic structure in the coarse grain.

The idea beneath the formulation (74–75) is illustrated in Fig. 12. As can be seen from this figure, the coarse scale FE model covers the entire model, and the atomistics are solved explicitly only on a selected region of interest. The atomic motion outside this domain is represented by the impedance boundary conditions according to (75). The reduced MD domain then evolves in time similarly, as if it was still a part of the full MD domain.

One issue relating to the formulation (75) is the large size of matrix $\mathbf{\Theta}$, which is typically $m \times m$, where m is number of atomistic degrees of freedom along the MD domain boundary. Each element of this matrix has to be calculated for a time large enough to capture the impedance effects accurately. This also requires a numerical inversion of the Laplace transform that can itself be computationally expensive. However, recent works by Karpov et al. [57] and Wagner et al. [58] have shown that exploiting the intrinsic symmetry and spatial repetitiveness of the atomistic structure in crystalline solids can drastically simplify and reduce the size and computational expense associated with these matrices. Based on Fourier analysis of periodic structures [135–137], this approach provides the impedance boundary conditions in terms of the lattice response functions, also known as the lattice dynamics Green's function in solid-state physics [138]. These functions provide a compact memory function, similar to $\mathbf{\Theta}$ of (75), to describe the renormalization of the interatomic interaction at the boundaries of the simulated domain. The matrices in the memory kernel are only $m_{\mathrm{B}} \times m_{\mathrm{B}}$, where m_{B} is at most the number of degrees of freedom in a Bravais lattice [139,140], i.e. one repetitive lattice cell. Though the original formalism (75) was derived assuming harmonic character of the atomic motion along the fine/coarse grain interface, the current form of the impedance force (75b) provides a reliable first-order approximation that treats moderately nonlinear interfaces satisfactorily [112,128]. Karpov and Liu [141] have shown that for stronger non-linearities, the performance of the impedance boundary conditions can be improved with an update based on the perturbation approach.

Finally, the quantum mechanical enrichment of the bridging scale formulation can be expressed, according to (33) and (75), as

$$\begin{aligned}
&\hat{H}\Psi = \left(U + \sum_{\alpha} E_{\alpha}\right)\Psi, \quad \mathbf{f}(\mathbf{u}) = -\frac{\partial U}{\partial \mathbf{u}}, \\
&\mathbf{M}_{\mathrm{A}}\ddot{\mathbf{q}} = \mathbf{f}(\mathbf{u}) + \int_0^t \mathbf{\Theta}(t-\tau)(\mathbf{q}(\tau) - \bar{\mathbf{u}}(\tau))\,\mathrm{d}\tau, \\
&\mathbf{M}\ddot{\mathbf{d}} = \mathbf{N}^{\mathrm{T}}\mathbf{f}(\mathbf{u}).
\end{aligned} \tag{75c}$$

This set of equations stands for the concurrent coupling of simulations at the three scales: subatomic, atomistic and continuum; in more details, see Ref. [143].

The dynamic bridging scale method with the impedance boundary conditions on the MD/continuum interface was applied by Park et al. [128] in studying wave propagation, and crack initiation and growth in the (1 1 1) plane of a face-centered cubic lattice structure governed by a two-body Lennard–Jones potential (18). Fig. 13 shows a comparison of the MD region displacements after a Gaussian-type wave with a combination of high and low frequency components that originated in the MD region has propagated into the surrounding continuum region.

By comparing the Fig. 13a and b, it is evident that if the high frequency waves emitted from the MD region are not treated in a mathematically rigorous manner, they reflect back from the MD/continuum (finite element) interface. The high frequency reflections are seen in the wake of the wave that has departed

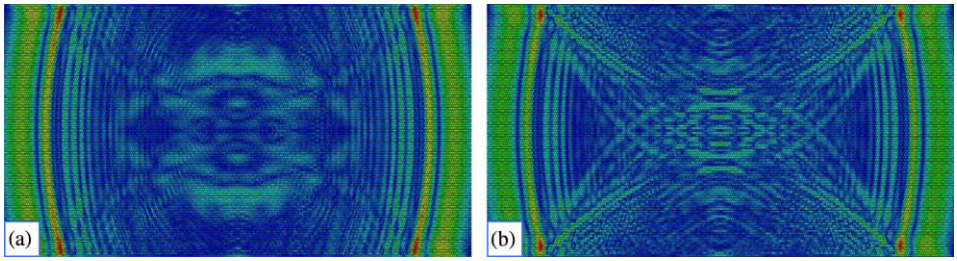

Fig. 13. Wave propagation through the atomistic domain in the FCC lattice structure: (a) impedance boundary conditions are involved at the MD/continuum interface, (b) continuity boundary conditions.

the MD region. These high frequency waves must be properly accounted for, particularly if they represent the majority of the initial energy of the MD system.

In the crack propagation problem, Fig. 14, considered by the same authors [128], the central part of the simulated domain initially contains anomalies in the regular crystal lattice that cause initiation and growth of a crack due to external in-plane loads. These loads are modeled with velocity boundary conditions applied to the boundaries of the coarse scale. Atomistic resolution is introduced in the area close to the crack. The coarse scale information eventually propagates into the MD region, and consequently the crack begins to propagate. Two snapshots of this process are given in Fig. 14a and b; the first snap shot captures initiation of the crack, and the second shows the configuration just before complete separation of the structure. Accuracy of the bridging scale simulation was verified by comparing it with a benchmark MD simulation, where the atomistic resolution was set throughout the entire coarse grain. The authors observed a very good agreement of the results: (1) the crack propagation speed was virtually identical in both cases; (2) the bridging scale model captures all specific details of the process within the fine grain, such as initiation and emission of the lattice dislocations away from the crack tip, see Fig. 14c.

For sufficiently large initial velocities, the authors observed complete fracture of the atomic lattice into two separate sections, depicted in Fig. 15. The multi-scale simulation of the entire region is shown in Fig. 15b, where the FE mesh is present everywhere, and MD model—in a smaller subsection of the total domain. The zoom Fig. 15c shows only the region in which both the FE and MD models exist, as opposed to the entire domain. The bridging scale simulation can be seen to agree very well with the benchmark MD simulation, Fig. 15a. It is also noteworthy that complete fracture of the underlying MD lattice is allowed in

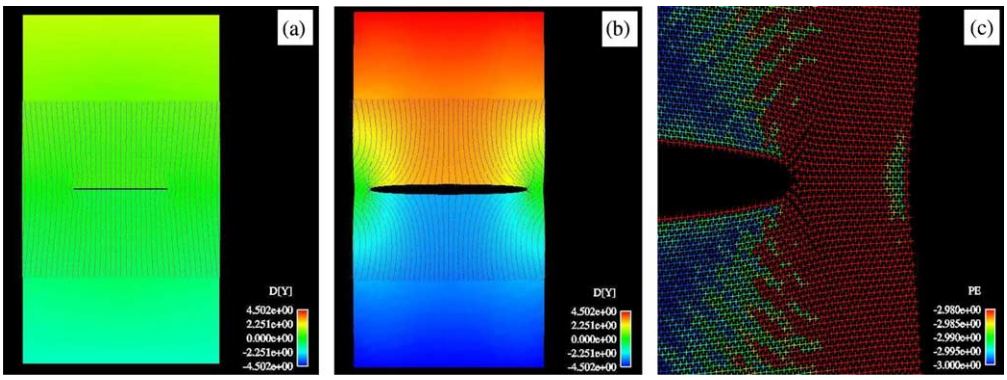

Fig. 14. Bridging multi-scale modeling of crack propagation: (a) initiation of a crack in the MD region, (b) pre-separation phase, (c) lattice dislocation pattern at the crack tip.

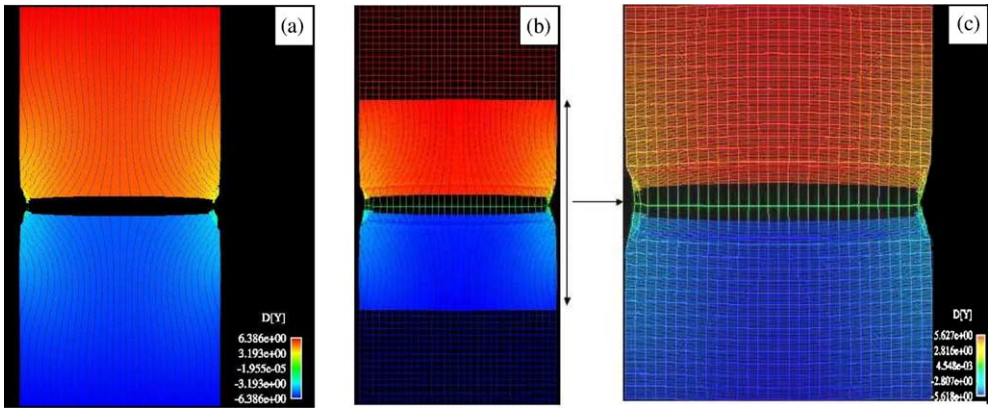

Fig. 15. Comparison of crack simulations at the lattice separation stage: (a) the full MD model, (b) the bridging multi-scale model. (c) The subdomain of coexisting of the MD and FE solutions (zoom in).

the coupled simulation—this is because the finite element simulation in that region is simply carried along by the MD simulation. The crack opening is shown in the Figs. 14a–b and 15 by magnifying the y-component of the displacement by a factor of three.

The bridging multi-scale formulation was also utilized in the context of fine scale enrichment of finite element models by Kadowaki and Liu [125]. The authors solved a two-dimensional dynamic shear strain localization problem, where a rectangular bar was discretized by the coarse-scale finite elements and only a small central region was discretized by the fine-scale finite elements. The edge length of the coarse-scale elements is eight times larger than that of the fine-scale elements. The bar is compressed by the impact velocity applied at both ends of the bar. Fig. 16 shows the effective plastic strain distribution of the coarse-scale FEM and the fine-scale FEM after the localized failure. The detail of the deformation in the shear-band is captured by the fine-scale FEM, while the computational cost is reduced by limiting the fine-scale FEM calculation near the failure region.

5.3.3. Temperature dependent processes

An important factor in multi-scale coupling is the need for a separate energy equation at the coarse scale. At the fine scale, there is no need for a separate concept of temperature or internal energy, since all of the dynamics are contained in the momentum equation for the atoms. However, in many problems of interest,

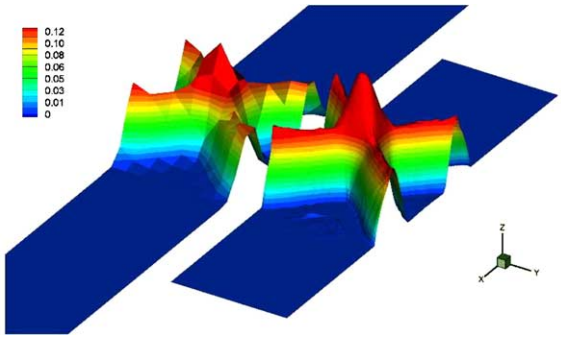

Fig. 16. Bridging multi-scale simulation of shear localization in a continuous bar.

a large amount of fine scale energy is generated in the region to be simulated with MD, and the propagation of this energy as heat into the coarse scale region is of great importance in accurately simulating the dynamics. At the boundaries of the fine scale region, the internal energy that passes out of the MD model should be tracked in the coarse scale region in an averaged sense through an energy equation

Formally, this averaging is done through an ensemble average. It has been shown by Wagner and Liu [129] that the ensemble average of the kinetic energy is

$$\langle K \rangle = \tfrac{1}{2}\dot{\mathbf{d}}^{\mathrm{T}}\mathbf{M}\dot{\mathbf{d}} + \tfrac{3}{2}k_{\mathrm{B}}T(N_{\mathrm{a}} - n_{\mathrm{c}}), \tag{76}$$

where k_{B} is Boltzmann constant, N_{a} is the number of atoms, n_{c} is the number of coarse scale nodes, and T is the temperature. The first term on the right-hand side is simply the coarse scale kinetic energy, while the second term can be thought of as the contribution of temperature to internal energy, i.e. the kinetic energy that is not represented by the coarse scale description. Clearly, this internal energy goes to zero in the limit as the number of coarse scale nodes approaches the number of atoms, i.e. as the coarse scale mesh approaches the atomic lattice size. This occurs because each node of the continuum mesh corresponds to an atom and the continuum mesh can then model the fine scale behavior.

An alternative approach was recently proposed by Park et al. [130], which is based on the microscopic definition of temperature. Using the projection operator technique, the authors derived a continuum (FE) temperature equation, which only requires information that is readily available from MD simulation, namely the MD velocities and atomic masses:

$$\sum_J M_{IJ} T_J = \frac{1}{k_{\mathrm{B}}} \sum_n N_I(\mathbf{X}_n) m_n^2 \dot{q}_n^2 b_n, \tag{77}$$

where the summation is performed over a discrete set of quadrature points X_n; M_{IJ} are the components of FE mass matrix, T are the nodal temperatures, and m, $\dot{q}$ and b are the representative FE mass, atomic velocity and quadrature weight associated with point X_n, respectively. At those locations, where no direct MD solution is available (the coarse continuum), the velocities were computed by means of an evolution kernel function w, as

$$\dot{q}_n(t) = \int_0^t \dot{w}_n(t-\tau) q_0(\tau)\,\mathrm{d}\tau, \tag{78}$$

where q_0 is the displacement at the atomistic/continuum interface. The kernel function w describes temporal and spatial evolution of atomic lattice dynamics, and its behavior solely depends on the atomic lattice geometry and on the form of the MD potential.

Eq. (77) was shown to give an accurate comparison to the actual MD temperature for a benchmark problem with the 1D monoatomic chain. Fig. 17 compares the temperature gradients for in a thermal wave propagation process: the first is computed based on the full atomistic resolution throughout the computational domain, and the second on the multi-scale temperature equation (77). One issue left for future research is to examine how the multi-scale heat conduction equations can be formulated for definitions of temperature posed according to (76) or (77) and (78).

5.4. Multi-scale boundary conditions

The key issue of a concurrent simulation approach is the coupling between the coarse and fine scales. An approximation is necessary along the fine-coarse grain interface, due to the fundamental incompatibility of the atomistic and continuum descriptions, e.g. [155]. This incompatibility is imposed by the mismatch of dispersion characteristics of the continuous and discrete media in dynamic simulations, and by non-local character of the atomic interaction in both dynamic and quasi-static simulations. Most of the concurrent approaches, excluding the bridging scale method, involve an artificial *handshake* or *pad* region [120], where

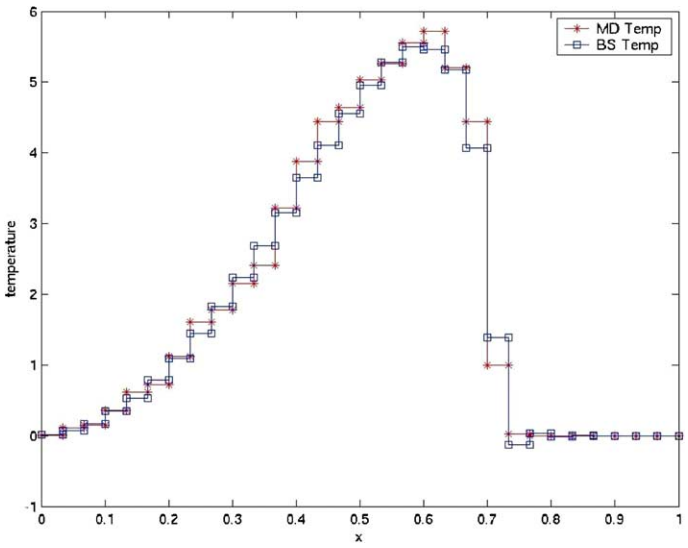

Fig. 17. Snapshot of temperature gradient in a 1D thermal wave propagation process; comparison made for the full atomistic resolution (red) and the bridging multi-scale model (blue).

pseudoatoms are available on the continuum part of the interface and share physical space with finite elements. At the front end of the continuum interface, the finite elements have to be scaled down the chemical or ion bond lengths; that may call forth costly inversions of large and ill-conditioned stiffness matrices.

The purpose of the handshake region is to assure a smoother coupling between the atomistic and continuum regimes. The group of pseudoatoms serves to eliminate the non-physical surface in the atomistic lattice structure, so that the real atoms along the interface have a full set of interactive neighbors in the continuum domain. In dynamic simulations, the handshake also serves as a damper/absorbent to reduce spurious reflection of high frequency phonons that cannot pass into the coarse scale domain. In both dynamic and quasi-static simulations, an extremely fine finite element mesh is required in order to provide accurate positions of the pseudoatoms, as those are dictated by interpolation from the finite element nodal positions [120].

An alternative methodology has been proposed recently by Karpov et al. [57,142] and Wagner et al. [58], where positions of actual next-to-interface atoms from the coarse grain are computed at the intrinsic atomistic level by means of a functional operator over the interface atomic displacements; that eliminates the need in a costly handshake domain. The sole purpose of a continuum model, when used in conjunction with multi-scale boundary conditions [128], is to represent effects of the peripheral (coarse grain) boundary conditions into the central atomistic region of interest. Provided that this effect is ignorable, at least in the analytical sense, the multi-scale boundary conditions can also serve as a self-contained multiple-scale method not to involve the Cauchy–Born rule and the consequent continuum model [142]. Atomistic resolution along the interface phase along with the intrinsic regularity of the internal structure of the crystalline solids allows calculating the structural response of the coarse scale on the atomistic level, based on a group of lattice mechanics techniques.

5.4.1. Quasi-static problems

The basic idea of the quasi-static multi-scale boundary conditions, proposed by Karpov et al. [142], is explained on the 1D example problem depicted in Fig. 18. The boundary atom $n = 0$ of the MD domain is

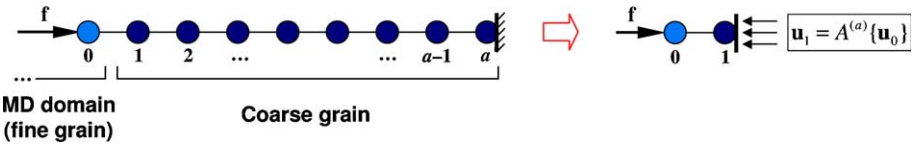

Fig. 18. An illustration to the concept of multi-scale boundary conditions: behavior of the MD boundary is governed by a deformable boundary equation, which accounts for the effect of a coarse scale domain.

subjected to a load due to some atomistic process on the left and the response of a coarse grain on the right. The solution for the interface atom can be computed, without solving the entire coarse scale, provided that a relationship between the displacements of atoms 1 and 0 is established,

$$\mathbf{u}_1 = A^{(a)}\{\mathbf{u}_0\}. \tag{79a}$$

Here, $A^{(a)}$ is a linear operator, whose form depends on the lattice properties and the coarse scale size parameter a. Only the first neighbor interaction is assumed in (79a) for clarity. More general coarse grain boundary conditions $\mathbf{u}_a \neq 0$, rather than the shown case $\mathbf{u}_a = 0$, may also contribute to this solution, so that

$$\mathbf{u}_1 = A^{(a)}\{\mathbf{u}_0, \mathbf{u}_a\}. \tag{79b}$$

Based on elementary arguments, one obtains, for the 1D problem depicted in Fig. 18,

$$\mathbf{u}_1 = \frac{a-1}{a}\mathbf{u}_0 + \frac{1}{a}\mathbf{u}_a. \tag{79c}$$

Relationships of the type (79) are referred to as the *multi-scale boundary conditions*. They are solved simultaneously with the MD equations for the fine grain to yield an atomistic solution, which incorporates effects of the adjacent coarse scale domain. The corresponding position of atom 1 can be also viewed as a *deformable* boundary of the MD domain.

For more general multi-dimensional problems, the multi-scale boundary conditions can be obtained with the use of the Fourier analysis of periodic structures [135–137]. This approach was verified on a benchmark nanoindentation problem with the 3D FCC gold lattice [142], as schematically shown in Fig. 19.

The bottom part of the substrate is considered as a bulk coarse scale that features almost homogeneous deformation patterns, and whose degrees of freedom can be eliminated from the explicit MD model. Periodic boundary conditions were applied along side-cut of the substrate. The atomic displacements along

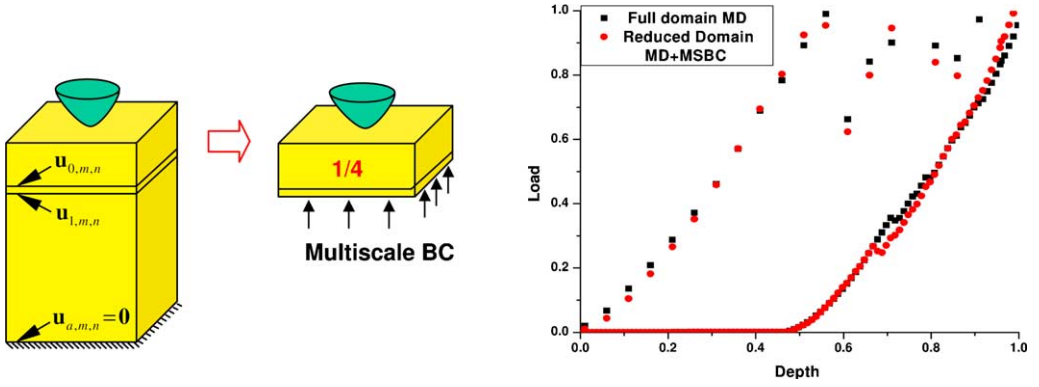

Fig. 19. Multi-scale boundary conditions for nanoindentation problems.

the deformable boundary layer in the reduced MD domain were co-related with the displacements of atoms in the adjacent layer through the discrete convolution operator

$$\mathbf{u}_{1,m,l} = A^{(a)}\{\mathbf{u}_{0,m,l}\} = \sum_{m',l'} \mathbf{\Theta}^{(a)}_{m-m',l-l'}\mathbf{u}_{0,m',l'}. \tag{80}$$

Here, the kernel matrix $\mathbf{\Theta}$ depends solely on the choice of the interatomic potential and the size of the coarse scale, and indexes m, l show numbering of atoms on the given layer. Eq. (80) involves no coarse scale boundary conditions $\mathbf{u}_{a,m,l}$ (along the bottom layer of the substrate), as those are usually set trivial in nanoindentation simulations.

The multi-scale boundary conditions according to (80) were shown to perform well for a wide range of the indentation depths, where a good agreement with the benchmark full domain solution was observed. Most importantly, the approach adequately reproduces the plasticity phenomena in the substrate around the indenter tip. Those result in the discontinuous character of the load/indentation depth curve depicted in Fig. 19. Coarse scale lattice defects caused by the nanoindentation process are not restrained, because the method formulation assumes spatial regularity of the lattice structure only in the immediate vicinity of each given atom on the deformable boundary layer.

5.4.2. Dynamic problems

The general dynamic formulation of the multi-scale boundary conditions is identical with the quasi-static case, i.e.

$$\mathbf{u}_1(t) = A^{(a)}\{\mathbf{u}_0(t), \mathbf{u}_a(t)\}, \tag{81a}$$

where $A^{(a)}$ is some functional linear operator.

In many dynamic problems, the coarse scale can often be viewed in the infinite sense, so that the effect of its boundary condition $\mathbf{u}_a$ is not present in the MD domain of interest. This situation is common for dynamic simulations due to the availability of a finite speed with which any mechanical excitation propagates through the molecular lattice as a progressive wave package. Recall that in such problems as the heat wave propagation from a localized source (Fig. 13), ion beam deposition (Fig. 5) and nanoindentation (Figs. 6 and 19), one observes the "one-way" wave flow from inside the domain of interest. Distant boundaries of a coarse grain domain then behave passively and usually remain stationary, unless the simulation time is large enough for the wave flow to reach the edges of the coarse grain. Due to physical arguments, and also for the sake of saving the computer efforts, it is then appropriate to assume that the progressive waves never reach the traction-free coarse scale boundaries, so that no inward flow of information occurs in the abovementioned problems, and

$$\mathbf{u}_1(t) = A\{\mathbf{u}_0(t)\}. \tag{81b}$$

Here, the operator A no longer depends on the coarse scale size parameter a. This form of the dynamic multi-scale boundary conditions is also referred to as the*impedance* boundary conditions.

From the knowledge of displacements $\mathbf{u}_0(t)$, $\mathbf{u}_1(t)$, and also the interatomic potential function, one can compute the force exerted by the coarse scale onto each given atom at the MD domain boundary. Note that this force will be analogous to the impedance force utilized within the dynamic bridging scale formulation (74)–(75).

As was shown by Karpov et al. [57] and Wagner et al. [58], the form of operator A is particularly compact for the MD/coarse grain interface with a regular crystalline structure and harmonic character of the motion. For a plane-like interface, it acts as a time convolution integral and discrete spatial summation over the interface degrees of freedom. For the 2D lattice problem depicted in Fig. 20,

$$\mathbf{u}_{1,m}(t) = \sum_{m'=m-m_c}^{m+m_c} \int_0^t \mathbf{\Theta}_{m-m'}(t-\tau)\mathbf{u}_{0,m'}(\tau)\,\mathrm{d}\tau, \tag{82}$$

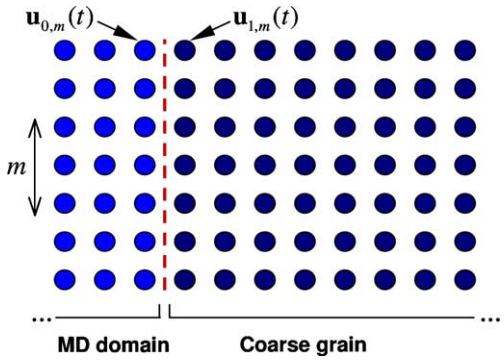

Fig. 20. Plane MD/coarse scale interface in a 2D cubic lattice. Index m shows atomic numbering along the interface.

where the impedance kernel function $\boldsymbol{\Theta}$ depends only on the form of the interatomic potential, and m_c is some critical difference $|m - m'|$ after which the summation is truncated. More complicated boundary shapes, such as a rectangle or parallelepiped, are assembled by combining several plane-like interfaces, where each face is treated according to (82). Calculation of the kernel matrix $\boldsymbol{\Theta}$ involves a Laplace transform inversion, which can be accomplished numerically based on Weeks [146], Papoulis [147], or other [148,149] algorithms. A crucial aspect is that the amplitude of this function decays in time and with the growth of the spatial parameter m, and it typically behaves as shown in Fig. 21.

The use of numeric Laplace inversion techniques [146–149] normally implies a limited range for the arguments of the computed functions of $\boldsymbol{\Theta}$ (82), from $t = 0$ to some critical value t_c for the difference $t - \tau$. Therefore it is important to investigate the effect of temporal truncation for the convolution integral in (82) at various t_c. However, such a truncation considerably decreases the computational cost and computer memory requirements.

Performance of the method, as depending on the choice the parameters m_c and t_c, was studied by Karpov et al. [57] on an example 2D cubic lattice. A square boundary shape for the lattice was chosen. Fig. 21

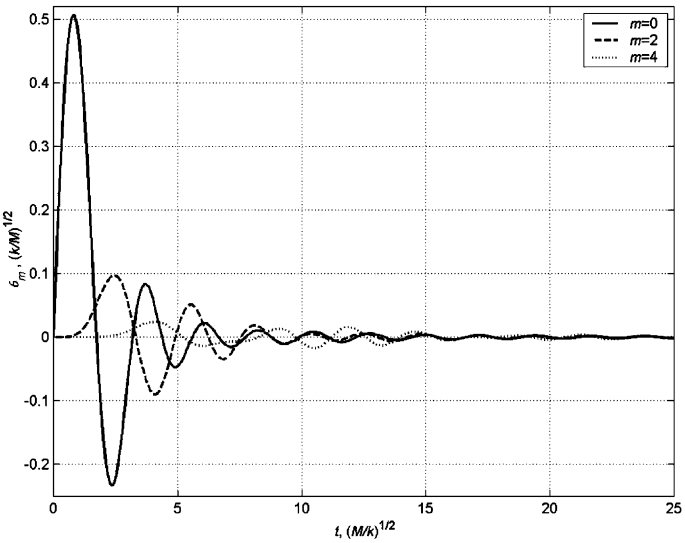

Fig. 21. Impedance kernel function for the 2D cubic lattice.

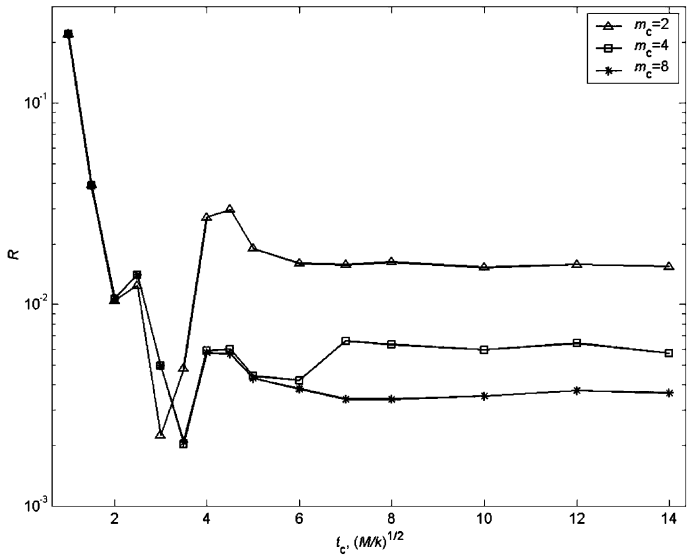

Fig. 22. Typical performance of the impedance boundary condition: dependence of the reflection coefficient on method parameters.

presents the impedance kernel computed for this lattice. The authors introduced the reflectivity coefficient R as a measure of efficiency of the boundary conditions (82). The value R gives the ratio between the kinetic energy of wave flow reflected by the MD/coarse grain interface and the energy of incident waves,

$$R = \frac{E^{\text{refl}}}{E^{\text{incid}}}. \tag{83}$$

In the ideal case of fully transparent boundary conditions, the value R is trivial. The results of the calculations are presented in Fig. 22. Analysis of Figs. 21 and 22 indicates that the use of 2 or 3 full oscillations of the kernel functions at $m_c = 4$ is sufficient to dissipate more than 99% of the incident kinetic energy at the MD/coarse scale interface.

As soon as the MD simulation is performed over a considerably small atomistic domain, the effect of surrounding media can be taken into account by utilizing the above techniques. Note that physical behavior and properties of simulated domains cannot be unambiguously attributed to a corresponding macro-scale system, unless the MD boundary conditions most rigorously describe this effect. In contrast to the heat bath technique, Section 4.2, the multi-scale boundary conditions represent the true physical behavior of the MD domain boundaries and accurately describe absorption of the thermal waves passing through MD/coarse grain interface.

5.4.3. Non-harmonic operator

The harmonic formulations for the multi-scale boundary conditions, outlined in Sections 5.4.1 and 5.4.2, satisfactorily treats weak non-linearities in the interface atomic behavior [112,128,142]. Stronger non-linearities can be treated with an update by Karpov and Liu [141] based on a perturbation approach, where the non-harmonic component is treated as a perturbation to the linear model. Within the non-harmonic settings, the functional operator A for (79) and (81) takes a more general form, rather than the simple convolution sum (80) and integrals (82). The perturbation approach enables one to accomplish a series expansion of this operator A. For the dynamic 1D system, for example, the first two terms in this expansion give the following:

$$A\{\mathbf{u}(t)\} = \int_0^t \mathbf{\Theta}_1(t-\tau_1)\mathbf{u}(\tau)\,\mathrm{d}\tau_1 + \int_0^t \int_0^t \mathbf{\Theta}_2(t,\tau_1,\tau_2)\mathbf{u}(\tau_1)\mathbf{u}(\tau_2)\,\mathrm{d}\tau_1\,\mathrm{d}\tau_2 + \cdots. \tag{84}$$

A two term expansion is expected to be sufficient for moderate non-linearities in the interface atomic behavior. Similar to the linear impedance matrix $\mathbf{\Theta}_1$, the second-order matrix $\mathbf{\Theta}_2$ solely depends on the lattice geometry and the form of interatomic potential. Other representations for the operator A may be possible, for example, based on successive iteration procedures, or on the exact solutions for non-linear lattice dynamics proposed by Toda [150]; these issues require further investigation.

5.5. Multi-scale fluidics: the immersed finite element method

The microscopic behavior of blood flow is essential in the performance of blood wetted artificial organs, where the designer's aim is to minimize biologically spurious processes, such as hemolysis and clotting. One determining mechanism of these processes is the aggregation of *red blood cells* (RBC), which can strongly influence the bio-mechanical properties of blood flow and blood's function in micro-vessels. Blood is a highly concentrated suspension of interacting and deformable RBCs, therefore the computer modeling of such a multi-phase material is rather challenging. In blood flow, one normally encounters a large range of length and time scales. Though the RBC has a diameter of about 10 μm, the interaction between neighboring RBCs typically involves nanoscale molecular forces.

Liu et al. [151] recently proposed a method of studying the phenomena of RBC aggregation, and its effect on the dynamic properties of blood flow. The method is based on coupling the Navier–Stokes equation with cell–cell interaction or protein molecular dynamics. The computer model to tackle the coupled fluid–solid system is derived from the Immersed Finite Element Method [152,153] and protein molecular dynamics. The authors consider a three-dimensional flexible structure completely immersed in a viscous fluid domain. The Eulerian and Lagrangian variables are adopted in the equations of motions for fluid and structural mechanics, respectively. In essence, a Lagrangian structural mesh is constructed to move on top of a background Eulerian fluid mesh. The coupling between the immersed solid and the surrounding fluid is accomplished by the discretized delta function (or mapping) between these two meshes.

An outline of the IFEM algorithm with the molecular cell–cell interaction is given as follows:

1. The fluid velocity and pressure are solved by the Eulerian fluid solver with an equivalent fluid–structure (fluid-RBC) interaction force $\mathbf{f}^{\mathrm{FSI}}$,

$$\rho^{\mathrm{f}}\left(\frac{\partial \mathbf{v}}{\partial t} + \mathbf{v}\cdot\nabla\mathbf{v}\right) = \nabla\cdot\boldsymbol{\sigma}^{\mathrm{f}} + \mathbf{f}^{\mathrm{FSI}}, \quad \nabla\cdot\mathbf{v} = 0.$$

2. The fluid–structure force vector is evaluated at the solid material points by the Lagrangian solid solver,

$$\mathbf{f}^{\mathrm{FSI,s}} = -(\rho^{\mathrm{s}} - \rho^{\mathrm{f}})^2\frac{\partial^2 v^{\mathrm{s}}}{\partial t^2} + \left(\frac{\partial \sigma^{\mathrm{s}}}{\partial x} - \frac{\partial \sigma^{\mathrm{f}}}{\partial x}\right) + (\rho^{\mathrm{s}} - \rho^{\mathrm{f}})g - \mathbf{f}^{\mathrm{C-C}},$$

where $\mathbf{f}^{\mathrm{FSI,s}}$ is the equivalent fluid–structure interaction force evaluated within the solid domain and the cell–cell interaction force is defined as the gradient of a molecular potential U,

$$\mathbf{f}^{\mathrm{C-C}} = \sum_i \mathbf{f}_i = -\sum_i \frac{\partial U}{\partial \mathbf{r}_i},$$

which is introduced to represent the protein dynamics between cell–cell contact.

3. Use RKPM window function as the discretized Dirac delta function to distribute fluid–structure interaction force onto the fluid equation,

$$\mathbf{f}^{\mathrm{FSI}}(\mathbf{x},t)=\int_{\Omega}\mathbf{f}^{\mathrm{FSI,s}}(\mathbf{X}^{\mathrm{s}},t)\phi(\mathbf{x}-\mathbf{x}^{\mathrm{s}})\,\mathrm{d}\Omega.$$

4. The same Dirac delta function is also employed for the computation of solid velocity,

$$\mathbf{v}^{\mathrm{s}}(\mathbf{X}^{\mathrm{s}},t)=\int_{\Omega}\mathbf{v}(\mathbf{x},t)\phi(\mathbf{x}-\mathbf{x}^{\mathrm{s}})\,\mathrm{d}\Omega.$$

The basic behavior of the interaction between two RBCs can be described such that weak attraction forces occur at far distances and strong repulsive forces occur at short distances. This aggregation process is modeled by utilizing a potential function, similar to the interatomic potential (17), though experimental study is required in order to identify the exact mechanism of RBC aggregation. The authors adopted the Morse potential (20), and quantitatively reproduced the aggregation behavior seen in experimental observation. Based on the experimental observation [154], the potential function is chosen such that the RBCs will de-aggregate at the shear rate of above 0.5 s^{-1}.

After the finite element discretization of the solid domain, the cell–cell interaction force $\mathbf{f}^{\mathrm{C-C}}$ is lumped at the solid nodes, as part of the nodal forces. This procedure is also applicable to non-uniform meshes.

As an illustrative example, Liu et al. [151] considered the RBCs passing through a vessel contraction, where the strong viscous shear introduced by such a flow contraction leads to the phenomena of RBC aggregation. It is shown in Fig. 23 that as RBCs pass the diffuser stage of the contraction, the deceleration of the RBCs forms blockage for the incoming RBCs. Therefore, dilation of RBCs is coupled with the pile-up of RBCs. Aggregation of RBCs is observed at the outlet of the narrower part of the vessel.

In the second example, the authors applied a shear flow on an RBC aggregate, which forms a single blockage pattern [151]. As shown in Fig. 24, the RBCs initially begin to rotate as a group. As the RBCs align themselves with the shear flow, the RBC aggregates start to peel off as the viscous shear forces cause disintegration of the RBC aggregates. When individual RBCs are separated from the other RBCs to a critical distance at which the cell–cell interaction forces become zero, the RBC aggregate becomes completely separated.

Three-dimensional simulations of a single red blood cell squeezing through a capillary vessel were also presented [151]. The RBC diameter is 1.2 times larger than that of the capillary vessel, which leads to the divergence of the cytoplasm (the liquid phase) to the two ends of the capsule by deforming into a slug during the squeezing process. During the exiting process, there is a radial expansion of the slug due to the convergence of the cytoplasm, which deforms the capsule into a jellyfish shape. In Fig. 25, four snapshots illustrate various stages of the red blood cell's passage through the capillary vessel. The driven pressure trend within the capillary vessel is presented in Fig. 26. The maximum level of the pressure corresponds to the initial stage of the plugged flow, when the deformable cell is entering the capillary vessel.

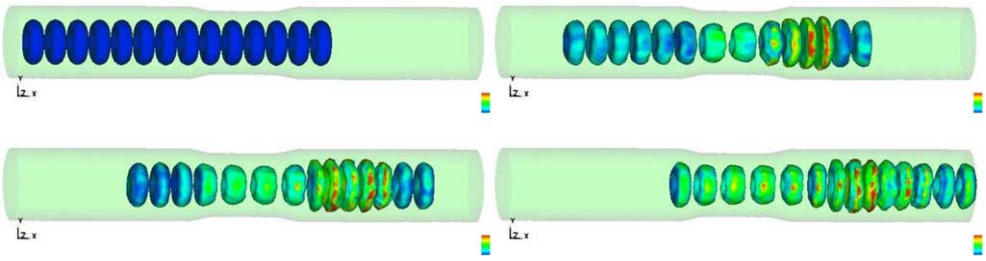

Fig. 23. The RBCs flow at 10 μm/s. at $t=0$ s, $t=2.0$ s, $t=4.0$ s, and $t=6.0$ s. The different colors indicate the value of stress exerted on RBCs. The aggregates of RBCs are clearly seen behind the narrow vessel.

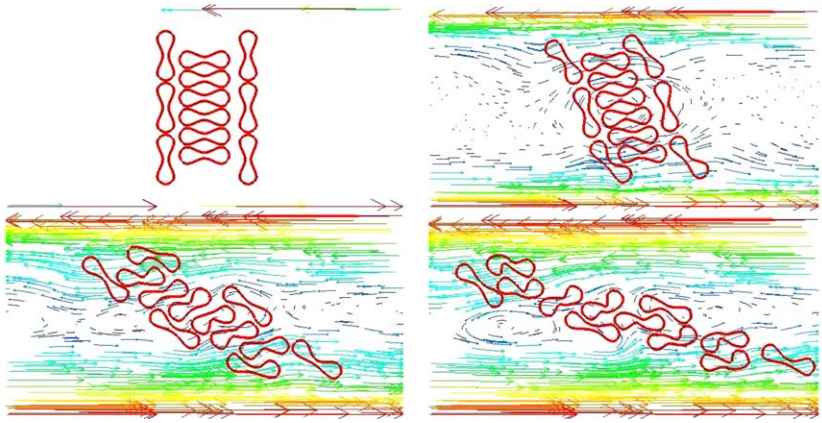

Fig. 24. The shear of 4 RBCs at the shear rate of 3.0 s^{-1}, at $t = 0$ s, $t = 1.0$ s, $t = 2.0$ s, and $t = 3.0$ s. The arrows show the fluid vortexes induced by the fluid-cell and cell–cell interactions.

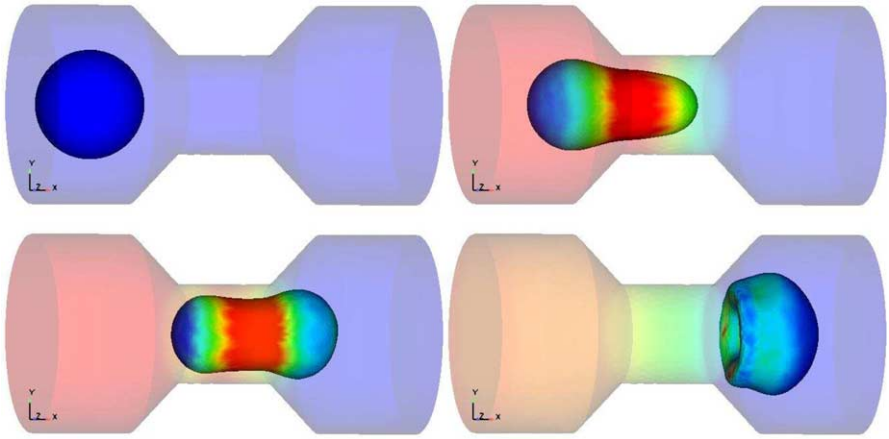

Fig. 25. Three-dimensional simulation of a single red blood cell (essentially a hollow sphere for simplicity) squeezing through a capillary vessel.

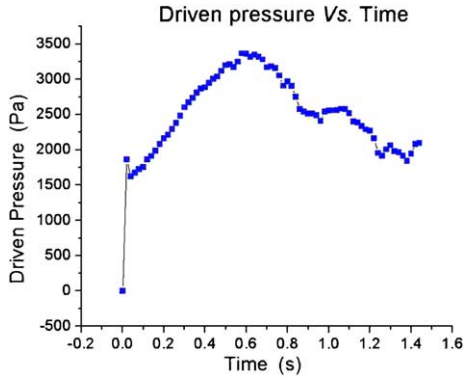

Fig. 26. The history of the driven pressure during the squeezing process.

6. Conclusion

We have reviewed the basic tools utilized in computational nanomechanics and materials, including the relevant underlying principles and concepts. These tools range from subatomic ab initio methods to classical molecular dynamics and multiple-scale approaches. The energetic link between the quantum mechanical and classical systems has been discussed, and limitations of the standing alone molecular dynamics simulations have been shown on a series of illustrative examples. The need for multi-scale simulation methods to tackle nanoscale aspects of material behavior was therefore emphasized; that was followed by a review and classification of the mainstream and emerging multi-scale methods. In this conclusion, we refer to Table 1, which summarizes the basic governing equations for various classes of the multiple-scale approaches.

In great generality, three major issues are still to be challenged by future researchers in the area of multiple-scale simulations. The first is to correctly account for the non-harmonic high frequency information that emanates from the molecular simulation when the information reaches the continuum. The second is the temperature dependent multi-scale formulations; in more details this issue is discussed in [128]. And the third is extending the time range currently available in standard MD simulations, so that the continuum and atomistic simulations may each evolve naturally on its natural time scale. It is noted that while the multi-scale methods reviewed in this work reduce the spatial computational requirements, they are still limited by the fact that MD simulations cannot be run for arbitrarily long periods of time. One of the efforts ongoing to relieve this restriction is the work by Voter and co-workers [156–158] on the so-called hyper molecular dynamics approach. This method appears well suited for problems in which the physical phenomena of interest occurs infrequently over long periods of time, with diffusion being a prime example. Other approaches have included the work by Huang et al. [159], in which thin film deposition in three dimensions is simulated by speeding up the surface diffusion of atoms.

Fundamental nanoscale research is being performed all around the world, and as this research is more and more being turned into viable engineering applications, our ability to model the performance of nanoscale structures remains limited. Continuum-based computational approaches are clearly not applicable over the full range of operational conditions for these nanoscale devices, as non-continuum behavior is observed in the large deformation behavior of carbon nanotubes, ion deposition processes, material mechanics, amongst many others.

More crucially, nanoscale components will likely be used in conjunction with components that are larger, and therefore have a mechanical response that is on much larger length and time scales than the nanoscale component. In such hybrid systems, typical single scale simulation methods such as molecular dynamics or quantum mechanics may not be applicable due to the disparity in length and time scales of the structure. For such systems, the computer-aided engineering tools must be able to span length scales from nanometers to microns, and time scales from femtoseconds to micro-seconds. Therefore, these systems cannot be modeled by continuum methods alone, because they are too small, or by molecular methods

Table 1
Summary of the multiple-scale formulations

	Subatomic/atomistic coupling	Atomistic/continuum coupling
Hierarchical	$U = E - \sum_\alpha E_\alpha, \quad \mathbf{M}\ddot{\mathbf{x}} = -\dfrac{\partial U}{\partial \mathbf{x}} \equiv \mathbf{f}(\mathbf{x})$	$\boldsymbol{\Sigma}_m = \boldsymbol{\Phi}_m(\boldsymbol{\Xi}_m, \boldsymbol{\eta}_{\text{T-S}}, \boldsymbol{\eta}_{\text{SP}})$ $\boldsymbol{\Sigma}_e = \boldsymbol{\Phi}_e(\boldsymbol{\Xi}_e, \boldsymbol{\eta})$
Concurrent	$\hat{H}\Psi = \left(U + \sum_\alpha E_\alpha\right)\Psi, \quad \mathbf{M}\ddot{\mathbf{x}} = -\dfrac{\partial U}{\partial \mathbf{x}}$	$\mathbf{M}_A\ddot{\mathbf{q}} = \mathbf{f}(\mathbf{u}) + \mathbf{f}^{\text{imp}}$ $\mathbf{M}\ddot{\mathbf{d}} = \mathbf{N}^{\text{T}}\mathbf{f}(\mathbf{u})$
Multi-scale BC	–	$\mathbf{u}_1 = A^{(a)}\{\mathbf{u}_0, \mathbf{u}_a\}$

alone, because they are too large. To support the design and qualification of nanostructured materials, a range of simulation tools must be available to designers just as they are today available at the macroscopic scales in general purpose software. However, considerable research is still required to establish the foundations for such software and to develop computational capabilities that span the scales from the atomistic to continuum. These capabilities should include a variety of tools, from finite elements to molecular dynamics and quantum mechanical methods, in order to provide powerful multi-scale methodologies. We hope that this work will be viewed as a step in the right direction in making the multi-scale goal a reality.

Nanotechnology will undoubtedly have a profound impact on the basic research being performed in medicine, electronics, materials science and many other areas in the upcoming years. However, in order to make nanotechnology a basic aspect of product design, it will be imperative that engineering software that can be used for nanoscale design be developed. Similar to the computer-aided design tools that are readily available for larger scale engineering simulations, we envision that nanoscale design tools will provide the engineer with similar capabilities in nanoengineering.

It is crucial that the knowledge underlying these recent developments in computational nanotechnology be transferred to scientists of today and tomorrow. We have developed two methods of disseminating this information. First, at Northwestern using NSF/IGERT funding we have created a new graduate program that is geared towards the application of molecular methods and their relation to and integration with continuum mechanics methods. These new courses, which include such topics as multi-scale simulations and their correlations to experiments and the application of surface science to nanomechanics and nanotribology, will ensure that the fundamental ideas presented in this work will be successfully passed down to the next generation of scientists and researchers.

Our second development is an NSF-sponsored summer institute on nanomechanics and materials, which was held for the first time at Northwestern in the summer of 2003. The goal of the summer institute is to bring together any interested scientists and engineers and expose them to lectures, hands-on laboratory experiments and simulation methods all taught by the leading researchers in nanotechnology today. It is hoped that the interest generated in nanotechnology by the summer institute will spur the bright minds in science and engineering to become the new leaders and innovators in this technologically crucial area of science.

Acknowledgements

This work was supported by the National Science Foundation (NSF), NSF-IGERT, NSF Summer Institute on NanoMechanics and Materials, Army Research Office and Office of Naval Research.

References

[1] T.J.R. Hughes, The Finite Element Method: Linear Static and Dynamic Finite Element Analysis, Prentice-Hall, Englewood Cliffs, New Jersey, 1987.
[2] O.C. Zienkiewicz, R.L. Taylor, The Finite Element Method, McGraw-Hill, London, New York, 1991.
[3] T. Belytschko, W.K. Liu, B. Moran, Nonlinear Finite Elements for Continua and Structures, John Wiley & Sons, Chichester, New York, 2000.
[4] S. Li, W.K. Liu, Meshfree and particle methods and their applications, Appl. Mech. Rev. 55 (2002) 1–34.
[5] W.K. Liu, S. Jun, Y.F. Zhang, Reproducing kernel particle methods, Int. J. Numer. Methods Fluids 20 (8–9) (1995) 1081–1106.
[6] T. Belytschko, Y.Y. Lu, L. Gu, Element-free Galerkin methods, Int. J. Numer. Methods Engrg. 37 (1994) 229–256.
[7] T. Belytschko, Y.Y. Lu, L. Gu, M. Tabarra, Element-free Galerkin methods for static and dynamic fracture, Int. J. Solids Struct. 32 (17) (1995) 2547–2570.
[8] W.K. Liu, S. Jun, S. Li, J. Adee, T. Belytschko, Reproducing kernel particle methods for structural dynamics, Int. J. Numer. Methods Engrg. 38 (1995) 1655–1679.

[9] W.K. Liu, S. Jun, D.T. Sihling, Y. Chen, W. Hao, Multiresolution reproducing kernel particle method for computational fluid dynamics, Int. J. Numer. Methods Fluids 24 (1997) 1391–1415.
[10] W.K. Liu, Y. Chen, Wavelet and multiple scale reproducing kernel methods, Int. J. Numer. Methods Fluids 21 (1995) 901–931.
[11] W.K. Liu, Y. Chen, C.T. Chang, T. Belytschko, Advances in multiple scale kernel particle methods, Computat. Mech. 18 (2) (1996) 73–111.
[12] F.C. Günther, W.K. Liu, Implementation of boundary conditions for meshless methods, Comput. Methods Appl. Mech. Engrg. 163 (1–4) (1998) 205–230.
[13] F.C. Günther, W.K. Liu, M.A. Christon, Multiscale meshfree parallel computations for viscous, compressible flows, Comput. Methods Appl. Mech. Engrg. 190 (2000) 279–303.
[14] W.K. Liu, Y.F. Zhang, M.R. Ramirez, Multiple scale finite element methods, Int. J. Numer. Methods Engrg. 32 (5) (1991) 969–990.
[15] I. Babuska, J.M. Melenk, The partition of unity method, Int. J. Numer. Methods Engrg. 40 (4) (1997) 727–758.
[16] W.K. Liu, R.A. Uras, Y. Chen, Enrichment of the finite element method with the reproducing kernel particle method, ASME J. Appl. Mech. 64 (1997) 861–870.
[17] D. Qian, G.J. Wagner, W.K. Liu, M.F. Yu, R.S. Ruoff, Mechanics of carbon nanotubes, Appl. Mech. Rev. 55 (6) (2002) 495–533.
[18] W.A. Goddard, D.W. Brenner, S.E. Lyshevski, G.J. Iafrate, Handbook of Nanoscience, Engineering and Technology, CRC Press, London, 2003.
[19] D. Qian, W.K. Liu, R.S. Ruoff, Mechanics of C60 in nanotubes, J. Phys. Chem. B 105 (2001) 10753–10758.
[20] D. Qian, W.K. Liu, R.S. Ruoff, Load transfer mechanism in carbon nanotube ropes, Compos. Sci. Technol. 63 (11) (2003) 1561–1569.
[21] D. Qian, W.K. Liu, S. Subramoney, R.S. Ruoff, Effect of interlayer interaction on the mechanical deformation of multiwalled carbon nanotube, J. Nanosci. Nanotechnol. 3 (1) (2003) 185–191.
[22] R.S. Ruoff, D. Qian, W.K. Liu, Mechanical properties of carbon nanotubes: theoretical predications and experimental measurements, Proceedings of the French Academy of Sciences, in press.
[23] M.F. Yu, M.J. Dyer, J. Chen, D. Qian, W.K. Liu, R.S. Ruoff, Locked twist in multi-walled carbon nanotube ribbons, Phys. Rev. B, Rapid Commun. 64 (2001) 241403R.
[24] O.A. Shenderova, V.V. Zhirnov, D.W. Brenner, Carbon nanostructures, Crit. Rev. Solid State 27 (3–4) (2002) 227–356.
[25] B.I. Yakobson, C.J. Brabec, J. Bernholc, Nanomechanics of carbon tubes: instabilities beyond linear response, Phys. Rev. Lett. 76 (14) (1996) 2511–2514.
[26] M.S. Dresselhaus, G. Dresselhaus, P.C. Eklund, Science of Fullerenes and Carbon Nanotubes, Academic Press, San Diego, 1996.
[27] P.J.F. Harris, Carbon Nanotube and Related Structures: New Materials for the 21st Century, Cambridge University Press, Cambridge, UK, 1999.
[28] B.I. Yakobson, R.E. Smalley, Fullerene nanotubes: C-1000000 and beyond, Am. Scientist 85 (4) (1997) 324–337.
[29] J. Bernholc, C. Brabec, M.B. Nardelli, A. Maiti, C. Roland, B.I. Yakobson, Theory of growth and mechanical properties of nanotubes, Appl. Phys. A—Mater. Sci. Process. 67 (1) (1998) 39–46.
[30] V.V. Pokropivnyi, Non-carbon nanotubes (review) II: types and structure, Powder Metall. Metal Ceram. 40 (11–12) (2001) 582–594.
[31] A. Zettl, Non-carbon nanotubes, Adv. Mater. 8 (5) (1996) 443.
[32] L.L. Beecrot, C.K. Ober, Nanocomposite materials for optical applications, Chem. Mater. 9 (6) (1997) 1302–1317.
[33] M. Alexandre, P. Dubois, Polymer-layered silicate nanocomposites: preparation, properties and uses of a new class of materials, Mater. Sci. Engrg. R 28 (1–2) (2000) 1–63.
[34] C. Wei, D. Srivastava, K. Cho, Thermal expansion and diffusion coefficients of carbon nanotube–polymer composites, Nanoletters 2 (6) (2002) 647–650.
[35] D. Qian, E.C. Dickey, R. Andrews, T. Rantell, Load transfer and deformation mechanisms in carbon nanotube–polystyrene composites, Appl. Phys. Lett. 76 (20) (2000) 2868–2870.
[36] M.S.P. Shaffer, A.H. Windle, Fabrication and characterization of carbon nanotube/poly(vinyl alcohol) composites, Adv. Mater. 11 (11) (1999) 937.
[37] G.M. Odegard, T.S. Gates, L.M. Nicholson, K.E. Wise, Equivalent-continuum modeling of nano-structured materials, Compos. Sci. Technol. 62 (14) (2002) 1869–1880.
[38] R. Andrews, D. Jacques, M. Minot, T. Rantell, Fabrication of carbon multiwall nanotube/polymer composites by shear mixing, Macromol. Mater. Engrg. 287 (6) (2002) 395–403.
[39] C.J. Kiely, J. Fink, J.G. Zheng, M. Brust, D. Bethell, D.J. Schiffrin, Ordered colloidal nanoalloys, Adv. Mater. 12 (9) (2000) 640.
[40] P. Moriarty, Nanostructured materials, Rep. Prog. Phys. 64 (3) (2001) 297–381.
[41] K.J. Bryden, J.Y. Ying, Thermal stability and hydrogen absorption characteristics of palladium–yttrium nanoalloys, Acta Mater. 44 (9) (1996) 3847–3854.

[42] N.T. Wilson, R.L. Johnston, A theoretical study of atom ordering in copper–gold nanoalloy clusters, J. Mater. Chem. 12 (10) (2002) 2913–2922.
[43] M.S.P. Sansom, P.C. Biggin, Water at the nanoscale, Nature 414 (2001) 156–159.
[44] D.T. Wasan, A.D. Nikolov, Spreading of nanofluids on solids, Nature 423 (2003) 156–159.
[45] E. Dujardin, T.W. Ebbesen, H. Hiura, K. Tanigaki, Capillarity and wetting of carbon nanotubes, Science 265 (1994) 1850–1852.
[46] P.A. Thompson, S.M. Troian, A general boundary condition for liquid flow at solid surfaces, Nature 389 (1997) 360–362.
[47] Y. Gogotsi, J.A. Libera, A.G. Yazicioglu, C.M. Megaridis, In situ multiphase fluid experiments in hydrothermal carbon nanotubes, Appl. Phys. Lett. 79 (7) (2001) 1021–1023.
[48] K. Koga, H. Tanaka, X.C. Zeng, First-order transition in confined water between high-density liquid and low-density amorphous phases, Nature 408 (2000) 564–567.
[49] J.M. Haile, Molecular Dynamics Simulation, Wiley & Sons, New York, 1992.
[50] M.P. Allen, D.J. Tildesley, Computer Simulation of Liquids, Oxford University Press, New York, 1987.
[51] W.G. Hoover, Molecular Dynamics, Springer-Verlag, Berlin, 1986.
[52] D.C. Rapaport, The Art of Molecular Dynamics Simulation, Cambridge University Press, New York, 1995.
[53] H.J.C. Berendsen, J.P.M. Postma, W.F. van Gunsteren, A. DiNola, J.R. Haak, Molecular dynamics with coupling to an external bath, J. Chem. Phys. 81 (8) (1984) 3684–3690.
[54] C. Schäfer, H.M. Urbassek, L.V. Zhigilei, B.J. Garrison, Pressure-transmitting boundary conditions for molecular dynamics simulations, Compos. Mater. Sci. 24 (2002) 421–429.
[55] W.E.Z. Huang, Matching conditions in atomistic-continuum modeling of materials, Phys. Rev. Lett. 87 (13) (2001) 135501.
[56] W. Cai, M. de Koning, V.V. Bulatov, S. Yip, Minimizing boundary reflections in coupled-domain simulations, Phys. Rev. Lett. 85 (15) (2000) 3213–3216.
[57] E.G. Karpov, G.J. Wagner, W.K. Liu, A Green's function approach to deriving wave-transmitting boundary conditions in molecular dynamics simulations, Compos. Mater. Sci., submitted for publication.
[58] G.J. Wagner, E.G. Karpov, W.K. Liu, Molecular dynamics boundary conditions for regular crystal lattices, Computer Methods in Applied Mechanics and Engineering: Special Issue on Multiscale Nano Mechanics and Materials, 2003.
[59] H. Goldstein, C.P. Poole, C.P. Poole Jr., J.L. Safko, Classical Mechanics, Addison Wesley, San Francisco, 2002.
[60] L.D. Landau, E.M. Lifshitz, Mechanics, Pergamon Press, Oxford, New York, 1978.
[61] J.E. Jones, On the determination of molecular fields. I. From the variation of the viscosity of a gas with temperature, Proc. Roy. Soc. A 106 (1924) 441–462.
[62] J.E. Jones, On the determination of molecular fields. II. From the equation of state of a gas, Proc. Roy. Soc. A 106 (1924) 463–477.
[63] Y. Wang, D. Tomanek, G.F. Bertsch, Stiffness of a solid composed of c60 clusters, Phys. Rev. B 44 (12) (1991) 6562–6565.
[64] R. Mahaffy, R. Bhatia, B.J. Garrison, Diffusion of a Butanethiolate molecule on a Au{1 1 1} surface, J. Phys. Chem. B 101 (1997) 771–773.
[65] F.H. Stillinger, T.A. Weber, Computer simulation of local order in condensed phases of silicon, Phys. Rev. B 31 (8) (1985) 5262–5271.
[66] T. Takai, T. Halicioglu, W.A. Tiller, Prediction for the pressure and temperature phase transitions of silicon using a semiempirical potential, Script. Metall. 19 (6) (1985) 709–713.
[67] R. Biswas, D.R. Hamann, Interatomic potential for silicon structural energies, Phys. Rev. Lett. 55 (19) (1985) 2001–2004.
[68] R. Biswas, D.R. Hamann, New classical models for silicon structural energies, Phys. Rev. B. 36 (12) (1987) 6434–6445.
[69] J. Tersoff, New empirical approach for the structure and energy of covalent systems, Phys. Rev. B 37 (12) (1988) 6991–7000.
[70] J. Tersoff, New empirical model for the structural properties of silicon, Phys. Rev. Lett. 56 (6) (1986) 632–635.
[71] J. Tersoff, Empirical interatomic potential for carbon, with applications to amorphous carbon, Phys. Rev. Lett. 61 (25) (1988) 2879–2882.
[72] D.W. Brenner, Empirical potential for hydrocarbons for use in simulating the chemical vapor deposition of diamond films, Phys. Rev. B 42 (15) (1990) 9458–9471.
[73] I. Rosenblum, J. Adler, S. Brandon, Multi-processor molecular dynamics using the Brenner potential: parallelization of an implicit multi-body potential, Int. J. Modern Phys. C 10 (1) (1999) 189–203.
[74] J.H. Los, A. Fasolino, Monte Carlo simulations of carbon-based structures based on an extended Brenner potential, Comput. Phys. Commun. 147 (1–2) (2002) 178–181.
[75] D.W. Brenner, O.A. Shenderova, J.A. Harrison, S.J. Stuart, B. Ni, S.B. Sinnott, A second-generation reactive empirical bond order (REBO) potential energy expression for hydrocarbons, J. Phys.: Condens. Matter 14 (2002) 783–802.
[76] M.W. Finnis, J.E. Sinclair, A simple empirical N-body potential for transition metals, Philos. Mag. A 50 (1) (1984) 45–55.
[77] T. Konishi, K. Ohsawa, H. Abe, E. Kuramoto, Determination of N-body potential for Fe–Cr alloy system and its application to defect study, Computat. Mater. Sci. 14 (1–4) (1999) 108–113.
[78] M.S. Daw, S.M. Foiles, M.I. Baskes, The embedded-atom method: a review of theory and applications, Mater. Sci. Rep. 9 (1993) 251–310.

[79] M.S. Daw, Model of metallic cohesion: the embedded-atom method, Phys. Rev. B 39 (11) (1989) 7441–7452.
[80] R.A. Johnson, Analytic nearest-neighbor model for fcc metals, Phys. Rev. B 37 (8) (1988) 3924–3931.
[81] D. Park, Introduction to the Quantum Theory, McGraw-Hill, New York, 1992.
[82] A.S. Davydov, Quantum Mechanics, Pergamon Press, Oxford, New York, 1965.
[83] P.A.M. Dirac, The Principles of Quantum Mechanics, Clarendon Press, Oxford, 1981.
[84] L.D. Landau, E.M. Lifshitz, Quantum Mechanics, Pergamon Press, London, Paris, 1959.
[85] M. Mueller, Fundamentals of Quantum Chemistry, Kluwer Academic/Plenum Publishers, New York, 2001.
[86] S.R. La Paglia, Introductory Quantum Chemistry, Harper & Row Publishers, New York, 1971.
[87] F.L. Pilar, Elementary Quantum Chemistry, McGraw-Hill, New York, 1990.
[88] K. Ohno, K. Esfarjani, Y. Kawazoe, Computational Materials Science: From Ab Initio to Monte Carlo Methods, Springer, Berlin, New York, 1999.
[89] F. Bloch, Über die quantenmechanik der elektronen in kristallgittern, Zeitschrift für Physik 52 (1928) 555–600.
[90] J.C. Slater, G.F. Koster, Simplified LCAO method for the periodic potential problem, Phys. Rev. 94 (6) (1954) 1498–1524.
[91] D.R. Hartree, The wave mechanics of an atom in with a non-Coulomb central field. Part I: Theory and methods, Proc. Cambridge Phil. Soc. 24 (1928) 89.
[92] V. Fock, Näherungsmethode zur Lösung des quantenmechanischen mehrkörperproblems, Zeitschrift für Physik 61 (1930) 126–148.
[93] E. Clementi, Ab initio computations in atoms and molecules, IBM J. Res. Dev. 44 (1–2) (2000) 228–245.
[94] P. Hohenberg, W. Kohn, Inhomogeneous electron gas, Phys. Rev. 136 (3B) (1964) 864–871.
[95] W. Kohn, J. Sham, Self-consistent equations including exchange and correlation effects, Phys. Rev. 140 (4A) (1965) 1133–1138.
[96] J.P. Perdew, E.R. McMullen, A. Zunger, Density-functional theory of the correlation energy in atoms and ions: a simple analytic model and a challenge, Phys. Rev. A 23 (6) (1981) 2785–2789.
[97] J.C. Slater, T.M. Wilson, J.H. Wood, Comparison of several exchange potentials for electrons in the Cu^+ ion, Phys. Rev. 179 (1) (1969) 28–38.
[98] V.L. Moruzzi, C.B. Sommers, Calculated Electronic Properties of Ordered Alloys, World Scientific Pub. Co., Singapore, 1995.
[99] R. Car, M. Parrinello, Unified approach for molecular dynamics and density functional theory, Phys. Rev. Lett. 55 (22) (1985) 2471–2474.
[100] M.C. Payne, M.P. Teter, D.C. Allan, T.A. Arias, J.D. Joannopoulos, Iterative minimization techniques for ab initio total-energy calculations: molecular dynamics and conjugate gradients, Rev. Mod. Phys. 64 (4) (1992) 1045–1097.
[101] VASP group, Vienna Ab-initio Simulation Package, Available from <http://cms.mpi.univie.ac.at/vasp>.
[102] H.P. Kaukonen, R.M. Nieminen, Molecular-dynamics simulation of the growth of diamond like films by energetic carbon-atom beams, Phys. Rev. Lett. 68 (5) (1992) 620–623.
[103] H.S.L. Zhang, H.T. Johnson, G.J. Wagner, W.K. Liu, K.J. Hsia, Stress generation mechanisms in carbon thin films grown by ion-beam deposition, Acta Mater. 51 (17) (2003) 5211–5222.
[104] M. Dao, N. Chollacoop, K.J. Van Vliet, T.A. Venkatesh, S. Suresh, Computational modeling of the forward and reverse problems in instrumented sharp indentation, Acta Mater. 49 (2001) 3899–3918.
[105] E.G. Herbert, G.M. Pharr, W.C. Oliver, B.N. Lucas, J.L. Hay, On the measurement of stress–strain curves by spherical indentation, Thin Solid Films 398 (2001) 331–335.
[106] N.I. Tymiak, D.E. Kramer, D.F. Bahr, T.J. Wyrobek, W.W. Gerberich, Plastic strain and strain gradients at very small indentation depths, Acta Mater. 49 (2001) 1021–1034.
[107] W.W. Gerberich, N.I. Tymiak, J.C. Grunlan, M.F. Horstemeyer, M.I. Baskes, Interpretations of indentation size effects, J. Appl. Mech. 69 (4) (2002) 433–442.
[108] P. Depondt, A. Ghazali, J.C.S. Levy, Self-locking of a modulated single overlayer in nanotribology simulation, Surf. Sci. 419 (1) (1998) 29–37.
[109] S. Zhang, G.J. Wagner, S.N. Medyanik, W.K. Liu, Y.H. Yu, Y.W. Chung, Experimental and molecular dynamics studies of friction behavior of hydrogenated carbon films, Surf. Coat. Technol., in press.
[110] F.F. Abraham, J.Q. Broughton, N. Bernstein, E. Kaxiras, Spanning the continuum to quantum length scales in a dynamic simulation of brittle fracture, Europhys. Lett. 44 (6) (1998) 783–787.
[111] J.Q. Broughton, F.F. Abraham, N. Bernstein, E. Kaxiras, Concurrent coupling of length scales: methodology and application, Phys. Rev. B 60 (4) (1999) 2391–2403.
[112] H.S. Park, W.K. Liu, An introduction and tutorial on multiple scale analysis in solids, Computer Methods in Applied Mechanics and Engineering: Special Issue on Multiscale Nano Mechanics and Materials, 2003.
[113] E.B. Tadmor, M. Ortiz, R. Phillips, Quasicontinuum analysis of defects in solids, Phil. Mag. A 73 (6) (1996) 1529–1563.
[114] E.B. Tadmor, R. Phillips, M. Ortiz, Mixed atomistic and continuum models of deformation in solids, Langmuir 12 (19) (1996) 4529–4534.
[115] V.B. Shenoy, R. Miller, E.B. Tadmor, R. Phillips, M. Ortiz, Quasicontinuum models of interfacial structure and deformation, Phys. Rev. Lett. 80 (4) (1998) 742–745.

[116] R. Miller, E.B. Tadmor, R. Phillips, M. Ortiz, Quasicontinuum simulation of fracture at the atomic scale, Model. Simul. Mater. Sci. Engrg. 6 (5) (1998) 607–638.
[117] M. Ortiz, A.M. Cuitino, J. Knap, M. Koslowski, Mixed atomistic continuum models of material behavior: the art of transcending atomistics and informing continua, MRS Bull. 26 (3) (2001) 216–221.
[118] J. Knap, M. Ortiz, An analysis of the quasicontinuum method, J. Mech. Phys. Solids 49 (9) (2001) 1899–1923.
[119] V. Shenoy, V. Shenoy, R. Phillips, Finite temperature quasicontinuum methods, Mater. Res. Soc. Symp. Proc. 538 (1999) 465–471.
[120] W.A. Curtin, R.E. Miller, Atomistic/continuum coupling in computational materials science, Model. Simulat. Mater. Sci. Engrg. 11 (2003) R33–R68.
[121] A.C. Eringen, Microcontinuum Field Theories, Springer, New York, 1999.
[122] P. Germain, Method of virtual power in continuum mechanics. 2. Microstructure, SIAM J. Appl. Math. 25 (3) (1973) 556–575.
[123] R. Chambon, D. Caillerie, T. Matsuchima, Plastic continuum with micro structure, local second gradient theories for geomaterials: localization studies, Int. J. Solids Struct. 38 (46–47) (2001) 8503–8527.
[124] P.M. Mariano, Multifield theories in mechanics of solids, Adv. Appl. Mech. 38 (2002) 1–93.
[125] H. Kadowaki, W.K. Liu, Bridging multi-scale method for localization problems, Comput. Methods Appl. Mech. Engrg., in press.
[126] Su Hao, W.K. Liu, G.B. Olson, B. Moran, F. Vereck, A hierarchical constitutive model for materials design, Comput. Methods Appl. Mech. Engrg., in this issue.
[127] D. Qian, G.J. Wagner, W.K. Liu, A multiscale projection method for the analysis of carbon nanotubes, Comput. Methods Appl. Mech. Engrg., in this issue.
[128] H.S. Park, E.G. Karpov, W.K. Liu, P.A. Klein, The bridging scale for two-dimensional atomistic/continuum coupling, Comput. Methods Appl. Mech. Engrg., in this issue.
[129] G.J. Wagner, W.K. Liu, Coupling of atomistic and continuum simulations using a bridging scale decomposition, J. Computat. Phys. 190 (2003) 249–274.
[130] H.S. Park, E.G. Karpov, W.K. Liu, A temperature equation for coupled atomistic/continuum simulations, Computer Methods in Applied Mechanics and Engineering: Special Issue on Multiscale Nano Mechanics and Materials, 2003.
[131] R.E. Rudd, J.Q. Broughton, Coarse-grained molecular dynamics and the atomic limit of finite elements, Phys. Rev. B 58 (10) (1998) R5893–R5896.
[132] R.E. Rudd, J.Q. Broughton, Concurrent coupling of length scales in solid state systems, Phys. Status Solidi B 217 (1) (2000) 251–291.
[133] S. Adelman, J. Doll, Generalized Langevin equation approach for atom/solid-surface scattering—collinear atom/harmonic chain model, J. Chem. Phys. 61 (10) (1974) 4242–4245.
[134] S. Adelman, J. Doll, Generalized Langevin equation approach for atom-solid-surface scattering—general formulation for classical scattering off harmonic solids, J. Chem. Phys. 64 (6) (1976) 2375–2388.
[135] E.G. Karpov, N.G. Stephen, D.L. Dorofeev, On static analysis of finite repetitive structures by discrete Fourier transform, Int. J. Solids Struct. 39 (16) (2002) 4291–4310.
[136] M. Ryvkin, M.B. Fuchs, B. Nuller, Optimal design of infinite repetitive structures, Struct. Optim. 18 (2–3) (1999) 202–209.
[137] E.G. Karpov, N.G. Stephen, W.K. Liu, Initial tension in randomly disordered periodic lattices, Int. J. Solids Struct. 40 (20) (2003) 5371–5388.
[138] A.A. Maradudin, E.W. Montroll, G.H. Weiss, I.P. Ipatova, Theory of Lattice Dynamics in the Harmonic Approximation, Academic Press, New York, 1971.
[139] W. Borchardt-Ott, Crystallography, Springer-Verlag, Berlin, New York, 1993.
[140] T.C.W. Mak, G.-D. Zhou, Crystallography in Modern Chemistry: A Resource Book of Crystal Structures, Wiley, New York, 1992.
[141] E.G. Karpov, W.K. Liu, A non-linear operator for impedance and multiscale boundary conditions in solids, in press.
[142] E.G. Karpov, H. Yu, H.S. Park, W.K. Liu, J. Wang, Multiscale boundary conditions in crystalline solids: theory and application to nanoindentation, Phys. Rev. B, submitted for publication.
[143] E.G. Karpov, W.K. Liu, On the concurrent multiscale coupling of quantum mechanical and molecular dynamics simulations of nanostructured materials, in preparation.
[144] F.F. Abraham, D. Brodbeck, W.E. Rudge, X. Xu, A molecular dynamics investigation of rapid fracture mechanics, J. Mech. Phys. Solids 45 (9) (1997) 1595–1619.
[145] F.F. Abraham, R. Walkup, H.J. Gao, M. Duchaineau, T.D. De la Rubia, M. Seager, Simulating materials failure by using up to one billion atoms and the world's fastest computer: brittle fracture, Proc. Natl. Acad. Sci. USA 99 (9) (2002) 5777–5782.
[146] W.T. Weeks, Numerical inversion of Laplace transforms using Laguerre functions, J. Assoc. Comput. Mach. 13 (3) (1966) 419–426.
[147] A. Papoulis, A new method of inversion of the Laplace transform, Quart. Appl. Math. 14 (1956) 405–414.

[148] B. Davies, B. Martin, Numerical inversion of the Laplace transform: a survey and comparison of methods, J. Computat. Phys. 33 (1979) 1–32.
[149] D.G. Duffy, On the numerical inversion of Laplace transforms: comparison of three new methods on characteristic problems from applications, ACM Trans. Math. Software 19 (3) (1993) 333–359.
[150] M. Toda, Theory of Non-linear Lattices, Springer-Verlag, Berlin, New York, 1981.
[151] Y. Liu, L.T. Zhang, X. Wang, W.K. Liu, Coupling of Navier–Stokes equations with protein molecular dynamics and its application to hemodynamics, in preparation.
[152] L.T. Zhang, A. Gerstenberger, X. Wang, W.K. Liu, Immersed finite element method, Comput. Methods Appl. Math. Eng., in press.
[153] X. Wang, W.K. Liu, Extended immersed boundary method using FEM and RKPM, Comput. Methods Appl. Mech. Engrg., in press.
[154] S. Chien, Clumping (reversible aggregation and irreversible agglutination) of blood cellular elements—electrochemical interactions between erythrocyte surfaces, Thrombosis Res. 8 (1976) 189–202.
[155] P.A. Deymier, J.O. Vasseur, Concurrent multiscale model of an atomic crystal coupled with elastic continua, Phys. Rev. B 66(13) (2002) Art. No. 134106.
[156] A.F. Voter, Hyperdynamics: accelerated molecular dynamics of infrequent events, Phys. Rev. Lett. 78 (20) (1997) 3908–3911.
[157] A.F. Voter, A method for accelerating molecular dynamics simulation of infrequent events, J. Chem. Phys. 106 (11) (1997) 4665–4677.
[158] A.F. Voter, F. Montalenti, T.C. Germann, Extending the time scale in atomistic simulation of materials, Ann. Rev. Mater.Res. 32 (2002) 321–346.
[159] H.C. Huang, G.H. Gilmer, T.D. Rubia, An atomistic simulator for thin film deposition in three dimensions, J. Appl. Phys. 84 (7) (1998) 3636–3649.